Review

Photoacoustic Imaging for Women's Gynecological Health: Advances and Clinical Prospects

Panangattukara Prabhakaran Praveen Kumar *, Dong-Kwon Lim *, Taeho Kim *

Posted Date: 16 March 2026

doi: 10.20944/preprints202603.1150.v1

Keywords: photoacoustic imaging; contrast agents; women's health; gynecological disorders; endometriosis; uterine disease; biomedical imaging; non-invasive diagnostics

 doi:10.20944/preprints202603.1150.v1

Review

Photoacoustic Imaging for Women's Gynecological Health: Advances and Clinical Prospects

Panangattukara Prabhakaran Praveen Kumar [1,*], Dong-Kwon Lim [2,3,*] and Taeho Kim [1,*]

[1] Department of Biomedical Engineering, Institute for Quantitative Health Science and Engineering, Michigan State University, East Lansing, Michigan 48824, United States

[2] KU-KIST Graduate School of Converging Science and Technology, Korea University145 Anam-ro, Seongbuk-gu, Seoul 02841, South Korea

[3] KIST Brain Research Institute, Korea Institute of Science and Technology5 Hwarang-ro 14-gil, Seongbuk-gu, Seoul 02792, South Korea

* Correspondence: pananga1@msu.edu (P.P.P.K.); dklim@korea.ac.kr (D.-K.L.); kimtae47@msu.edu (T.K.)

Abstract

Photoacoustic imaging (PAI) is an emerging hybrid biomedical imaging modality that combines the high molecular contrast of optical excitation with the deep tissue penetration of ultrasound detection. This review presents recent advances in PAI-based techniques for the detection and characterization of gynecological and gynecological diseases in women, with particular focus on endometriosis and uterine-related disorders. We summarize the application of PAI across preclinical and translational studies, highlighting progress in photoacoustic microscopy, spectroscopic photoacoustic imaging, and endoscopic and probe-based implementations for noninvasive, high-resolution tissue evaluation. The role of functional and contrast-enhanced PAI approaches is discussed, emphasizing their ability to enhance diagnostic sensitivity, enable longitudinal monitoring, and provide detailed information on vascular, biochemical, and structural tissue characteristics. Furthermore, the expanding applications of PAI in assessing uterine, cervical, and ovarian pathologies, including tumor detection and tissue remodeling, are reviewed. Finally, current challenges, limitations, and future directions toward clinical translation are addressed. Collectively, this review underscores the potential of photoacoustic imaging as a powerful, noninvasive platform for early diagnosis, disease monitoring, and improved management of women's health conditions.

Keywords: photoacoustic imaging; contrast agents; women's health; gynecological disorders; endometriosis; uterine disease; biomedical imaging; non-invasive diagnostics

1. Introduction

Gynecological disorders represent a significant and often underrecognized health burden among women of reproductive age, largely due to their gradual onset, nonspecific clinical symptoms, and frequent recurrence [1,2]. Conditions such as endometriosis [3–5], uterine abnormalities [6,7], and ovarian pathologies [8,9] can progress silently over long periods before becoming clinically evident, at which stage treatment options are often more invasive or limited. Delayed diagnosis not only increases disease severity but also adversely affects fertility, quality of life, and long-term reproductive health outcomes [10,11].

Current diagnostic approaches rely primarily on conventional imaging modalities, including ultrasound and magnetic resonance imaging (MRI), often complemented by invasive procedures such as laparoscopy and biopsy for definitive confirmation [12,13]. Although these methods provide valuable anatomical information, they frequently lack sensitivity to early-stage functional, biochemical, and microvascular alterations that precede visible structural changes [14]. Consequently, many gynecological diseases are identified only after substantial progression, reducing opportunities for early intervention and personalized therapeutic strategies.

 doi:10.20944/preprints202603.1150.v1

In response to these limitations, there is an increasing demand for noninvasive imaging technologies capable of detecting early pathological changes and guiding clinical decision-making [15]. Photoacoustic imaging (PAI), also known as photoacoustic tomography (PAT), has emerged as a promising modality that addresses this need by enabling functional and molecular-level tissue assessment at deep penetration depths of 5 – 7 cm [16]. By combining optical absorption contrast with ultrasonic spatial resolution, PAI allows visualization of vascular remodeling, tissue oxygenation, and biochemical alterations associated with early disease development [17,18]. This capability positions PAI not only as a diagnostic tool but also as a platform for treatment guidance and longitudinal monitoring, facilitating timely intervention and evaluation of therapeutic response.

With ongoing advances in bioengineering and imaging technology, photoacoustic systems hold substantial potential to transform the clinical management of gynecological disorders by shifting the diagnostic paradigm from late-stage detection toward early diagnosis, targeted therapy, and improved patient outcomes [19–21]. In this review, we summarize recent progress in PAI technologies for the early detection, characterization, and treatment monitoring of gynecological diseases, with particular emphasis on their translational relevance to women's health.

2. Basic Principle and Fundamentals of Photoacoustic Imaging

2.1 Basic Principle of Photoacoustic Signal Generation

PAI is a hybrid optical–acoustic imaging modality that enables high-contrast visualization of biological tissues by converting absorbed optical energy into ultrasonic signals. Upon nanosecond-pulsed laser-light irradiation, photoabsorbing molecules undergo rapid nonradiative relaxation, resulting in localized temperature increases that induce transient thermoelastic expansion and generate acoustic pressure waves [22]. These ultrasound signals propagate through tissue and are detected by ultrasonic transducers, allowing image reconstruction based on signal intensity and time-of-flight characteristics (**Figure 1A**) [23]. In contrast to conventional ultrasound imaging, which relies primarily on differences in mechanical impedance, PAI exploits variations in optical absorption, thereby providing enhanced contrast for imaging chromophores within complex biological environments. Compared with purely optical imaging techniques, PAI achieves substantially greater penetration depths extending to several centimeters while maintaining micrometer-scale spatial resolution. Photoacoustic contrast can originate from endogenous absorbers, such as hemoglobin and melanin, or from exogenously administered agents including organic dyes, fluorophores, and nanostructured materials (**Figure 1B**) [24,25]. However, endogenous chromophores are often present at limited or heterogeneous concentrations, which can restrict sensitivity and reproducibility. Consequently, exogenous contrast agents are frequently employed to amplify photoacoustic signals and improve imaging reliability (**Figure 1C**) [26].

The initial pressure rise (P_0) generated during photoacoustic signal formation can be described by the following relationship:

$$P_0 = \Gamma \eta_{th} \mu_a F \quad (1)$$

where Γ denotes the Grüneisen parameter describing the efficiency of thermoelastic conversion, η_{th} corresponds to the fraction of absorbed optical energy converted into heat, μ_a represents the optical absorption coefficient of the photoabsorber, and F is the local optical fluence. This expression highlights that photoacoustic signal intensity is determined by both the absorption efficiency and photothermal conversion capability of the contrast agent. Accordingly, the rational design of photoacoustic probes, particularly organic dyes and dye-based nanomaterials, that exhibit strong absorption and high photothermal efficiency, is critical for optimizing PAI performance.

Beyond structural imaging, PAI effectively addresses key limitations of traditional optical techniques by minimizing photon scattering in biological tissues, enabling high- resolution imaging at deep-tissue penetration [27–29]. A distinctive advantage of PAI is its ability to perform multi-wavelength spectroscopic imaging, which allows quantitative assessment of physiologically important parameters such as tissue oxygenation [30], vascular dynamics [31], and metabolic

 doi:10.20944/preprints202603.1150.v1

activity[32]. Furthermore, PAI can be readily integrated with other imaging modalities, including ultrasound and fluorescence imaging, enabling multimodal and multiscale imaging platforms that span spatial resolutions from the cellular level to whole organs [33,34]. Its rapid data-acquisition capability also facilitates real-time monitoring of dynamic biological processes, such as blood perfusion and drug distribution.

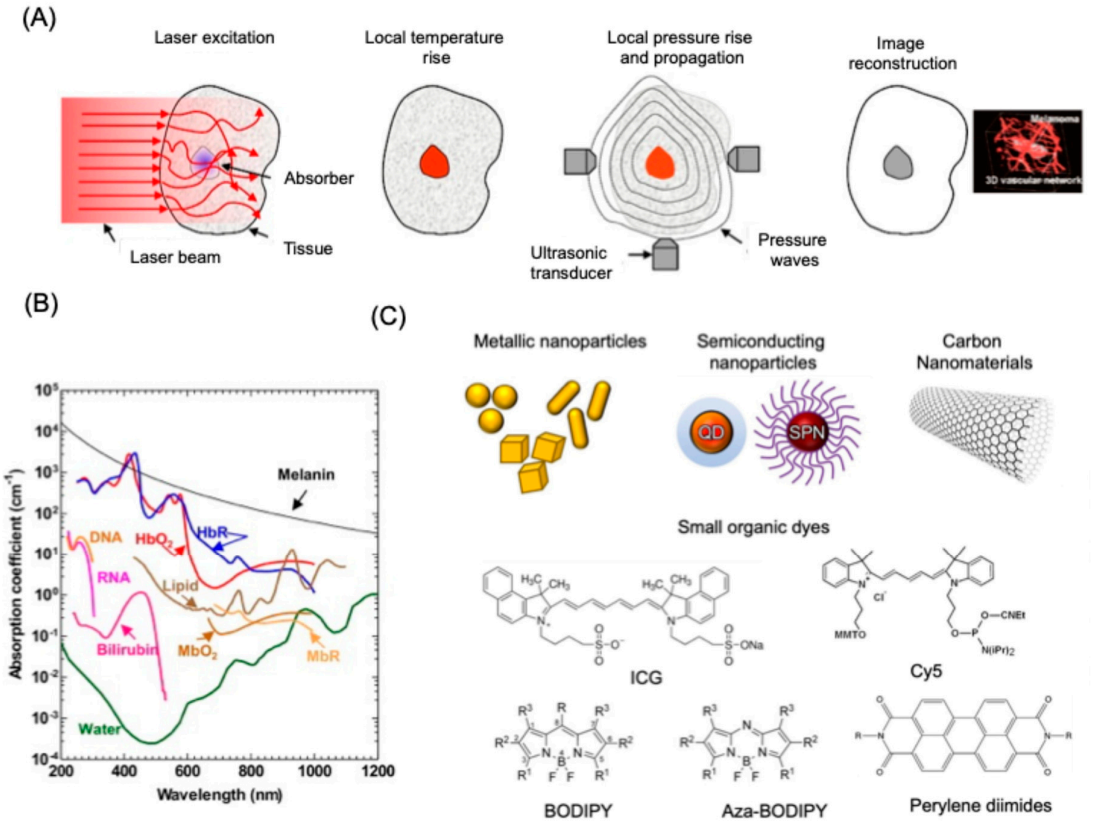

Figure 1. Basic principle for PAI. (A) Illustration of the fundamental working mechanism and image reconstruction process of PAI, along with a representative reconstructed photoacoustic image demonstrating melanoma visualization. Reproduced with permission from [23]. Copyright 2016, Nature Publishing Group. (B) Absorption spectra of key endogenous chromophores present in biological tissues at physiologically relevant concentrations are shown. These include oxyhemoglobin (HbO_2) and deoxyhemoglobin (HbR) at approximately 150 g/L in blood, lipids comprising about 20% tissue volume, and water representing nearly 80% of tissue composition. Additional absorbers include nucleic acids (DNA and RNA) at ~1 g/L within cell nuclei, melanin at roughly 14.3 g/L in average human skin, reduced and oxygenated myoglobin (MbR and MbO_2) at approximately 0.5% by mass in skeletal muscle, and bilirubin at a concentration of about 12 mg/L in blood. Reproduced with permission from [24]. Copyright 2014, Elsevier. (C) Pictorial representation for the commonly used exogenous contrast agents for PAI.

Owing to these advantages, PAI has emerged as a valuable tool in both preclinical and clinical biomedical research, with demonstrated applications in oncology[35], neurology[36], vascular biology[37], and inflammatory diseases[38]. In cancer imaging, PAI provides access to functional features of the tumor microenvironment that are difficult to capture using conventional imaging approaches alone. These include vascular morphology, perfusion patterns, and oxygenation heterogeneity, all of which are closely associated with tumor progression, therapeutic resistance, and disease outcome. By leveraging the distinct optical absorption spectra of oxygenated and deoxygenated hemoglobin, PAI enables noninvasive assessment of tissue hypoxia, a hallmark of aggressive and treatment-resistant tumors. Additionally, single-wavelength imaging strategies can

 doi:10.20944/preprints202603.1150.v1

be employed to visualize tumor-associated vasculature [39] and monitor angiogenic remodeling[40], while quantitative parameters such as vessel density [41], diameter [42], and geometric complexity serve as imaging-derived biomarkers for longitudinal disease evaluation [27].

2.2. Imaging Configurations

Depending on the imaging depth, resolution and application context, PAI uses multiple imaging configurations. These configurations broadly include photoacoustic microscopy, photoacoustic computed tomography, and endoscopic or probe-based photoacoustic systems, each offering distinct advantages for biological and biomedical investigations.

2.2.1. Photoacoustic Microscopy (PAM)

Photoacoustic microscopy (PAM) represents a high-resolution implementation of PAI designed to visualize biological structures within shallow to moderate tissue depths [43]. In PAM, imaging is performed in optical regimes where light propagation is partially ballistic or weakly diffusive, enabling detailed visualization of micro-scale features. PAM is generally characterized by spatial resolutions finer than tens of micrometers, well below the resolving capability of the unaided human eye. A defining distinction between PAM and photoacoustic computed tomography lies in the image formation strategy: PAM typically employs a focused, single-element ultrasound detector to acquire spatially resolved signals, whereas tomographic approaches rely on multi-element detector arrays and computational reconstruction algorithms.

The spatial resolution of PAM is governed by both optical excitation and acoustic detection parameters. Lateral resolution arises from the combined influence of the illumination profile, and the acoustic point spread function, while axial resolution is dictated primarily by the bandwidth of the ultrasound transducer. Based on the dominant contributor to lateral resolution, PAM systems are commonly categorized into optical-resolution PAM (OR-PAM) and acoustic-resolution PAM (AR-PAM) [17,43]. In OR-PAM, the excitation beam is tightly focused to a diffraction-limited spot that is significantly smaller than the acoustic focal zone, making the optical focus the primary determinant of lateral resolution. As a result, OR-PAM achieves exceptionally fine spatial resolution but is restricted to superficial imaging depths due to strong optical scattering in tissue (**Figure 2A**)[44,45]. Conversely, AR-PAM employs a broader optical illumination that encompasses the acoustic focal region, with lateral resolution primarily defined by ultrasonic focusing. This configuration allows imaging at deeper penetration with reduced sensitivity to optical scattering, at the cost of spatial resolution (**Figure 2B**)[46]. As illustrated in **Figure 2C**, an in vivo scan was performed on the dorsal region of an athymic nude mouse. Optical-resolution (OR) and acoustic-resolution (AR) PAM (**Figure 2D and 2E**) were collected simultaneously during a single scanning session, using step sizes of 2 μm and 20 μm and laser pulse repetition rates of 20 kHz and 2 kHz, respectively. The AR-PAM image captured prominent, deeper blood vessels but resolved fewer superficial microvessels compared with the OR-PAM image. In contrast, OR-PAM provided high-resolution visualization of small, shallow vasculature that was not clearly detected in AR mode. The combined image from **Figure 2F**, integrates both datasets, revealing superficial microvascular details from OR-PAM alongside deeper vascular structures from AR-PAM [47].

 doi:10.20944/preprints202603.1150.v1

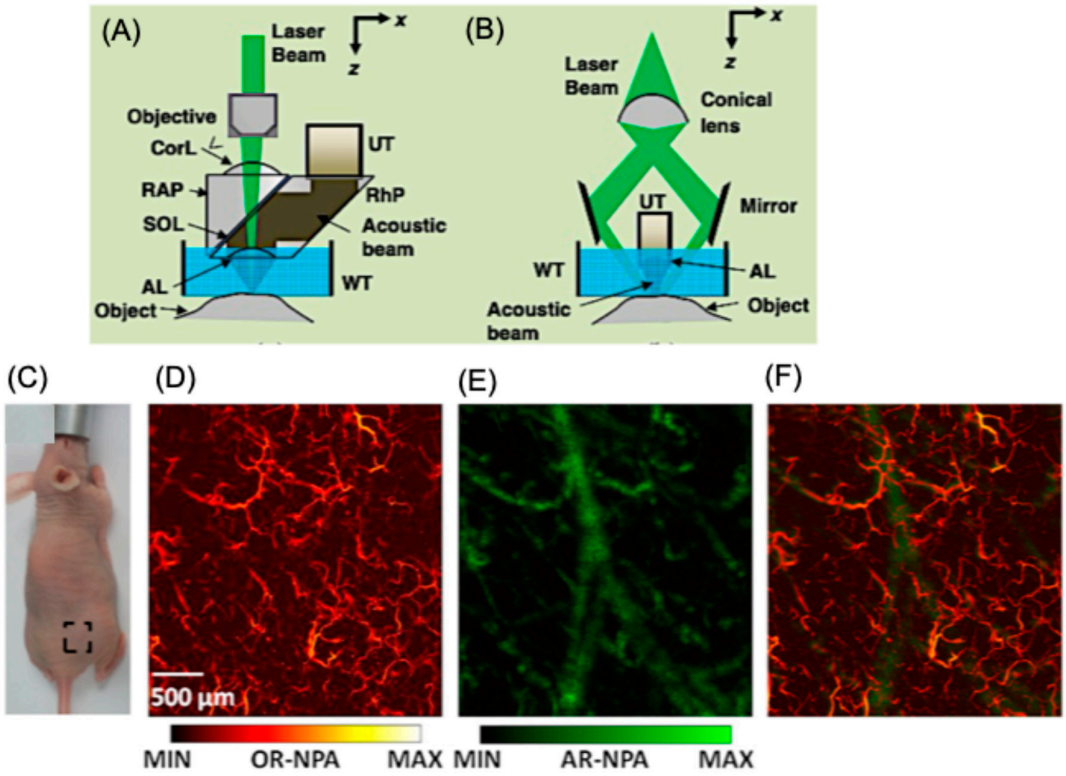

Figure 2. Optical Resolution Photoacoustic microscopy for in vivo imaging. (A) Schematic illustration of a second-generation optical-resolution photoacoustic microscopy (2G-OR-PAM) system, in which lateral spatial resolution is governed by diffraction-limited optical focusing. Components include an acoustic lens (AL), correction lens (CorL), right-angled prism (RAP), rhomboid prism (RhP), silicone oil layer (SOL), ultrasonic transducer (UT), and water tank (WT). (B) Configuration of dark-field acoustic-resolution photoacoustic microscopy (AR-PAM), where lateral resolution is primarily defined by diffraction-limited acoustic focusing. (C) Photograph of the mouse indicating the selected imaging area outlined by a dashed box. (D) Optical-resolution PAM (OR-PAM) image showing superficial skin vasculature. (E) Acoustic-resolution PAM (AR-PAM) image highlighting deeper vascular structures. (F) Merged PAM image combining both datasets. OR-NPA represents the normalized photoacoustic amplitude obtained from the OR-PAM image, while AR-NPA denotes the normalized photoacoustic amplitude from the AR-PAM image. Reproduced with permission from [47]. Copyright 2013, Optica Publishing Group.

PAM architectures can be further adapted for internal organ imaging applications through miniaturization, leading to the development of photoacoustic endoscopy (PAE). These systems often utilize rotational or linear scanning mechanisms and can operate in either optical- or acoustic-resolution modes, depending on the design of the illumination and detection components. By systematically adjusting optical parameters such as numerical aperture and excitation wavelength, or acoustic parameters including transducer frequency and focusing geometry, PAM platforms can be tuned across a wide range of resolutions and penetration depths. This scalability makes PAM a versatile tool for studying microvascular structures, tissue morphology, and functional biomarkers.

2.2.2. Photoacoustic Computed Tomography (PACT)

In photoacoustic computed tomography (PACT), image formation relies on mechanical or electronic scanning of multi-element ultrasound detector arrays, followed by computational reconstruction of the acquired signals [17]. Unlike photoacoustic microscopy (PAM), where signals arise from a spatially confined focal volume and can be directly mapped along the acoustic axis, PACT detectors possess broad angular sensitivity and require data integration from multiple elements to reconstruct an image. Based on detector arrangement, PACT systems are commonly

 doi:10.20944/preprints202603.1150.v1

categorized into planar, cylindrical, and spherical geometries, each offering distinct imaging capabilities.

Planar-view PACT systems typically employ two-dimensional piezoelectric transducer arrays or optical sensors such as Fabry–Perot interferometers, enabling wide-field signal acquisition (**Figure 3A**) [48]. While optical interferometric detectors offer high sensitivity and fine spatial sampling, their sequential readout can limit imaging speed compared to array-based approaches. An example of in vivo abdominal imaging obtained using a Fabry–Perot interferometer–based PACT system is illustrated in **Figure 3B**. The image clearly delineates two developing embryos (red color), together with surrounding uterine blood vessels and overlying skin structures, demonstrating the capability of this approach to resolve both anatomical and vascular features in a pregnant mouse model [48]. Cylindrical-view PACT, often implemented using ring-shaped transducer arrays, provides efficient cross-sectional imaging and can be extended to three-dimensional visualization through axial scanning (**Figure 3C**) [49,50]. This configuration is particularly suitable for rapid two-dimensional imaging of dynamic physiological processes and for visualizing vascular structures within deep tissues. **Figure 3D** illustrates the configuration of a ring-array–based small-animal imaging platform along with representative reconstructed images [49]. Organs with high vascular content, including the liver, spleen, spine, kidneys, and gastrointestinal tract, are distinctly visualized. Fine vascular networks within these structures are also resolved, demonstrating the system's capability for high-resolution angiographic imaging.

Spherical-view PACT systems employ transducer arrays arranged over curved geometries to achieve near-isotropic spatial resolution within the central imaging volume [51,52]. Although these systems can deliver high-quality volumetric images, they typically require mechanical scanning and full data acquisition prior to image reconstruction, which can limit real-time imaging performance. Recent advances in reconstruction algorithms have partially alleviated these limitations by enabling dynamic imaging from sparsely sampled datasets [27]. Collectively, the flexibility of PACT detection geometries allows the technique to be adapted for diverse preclinical and translational imaging applications.

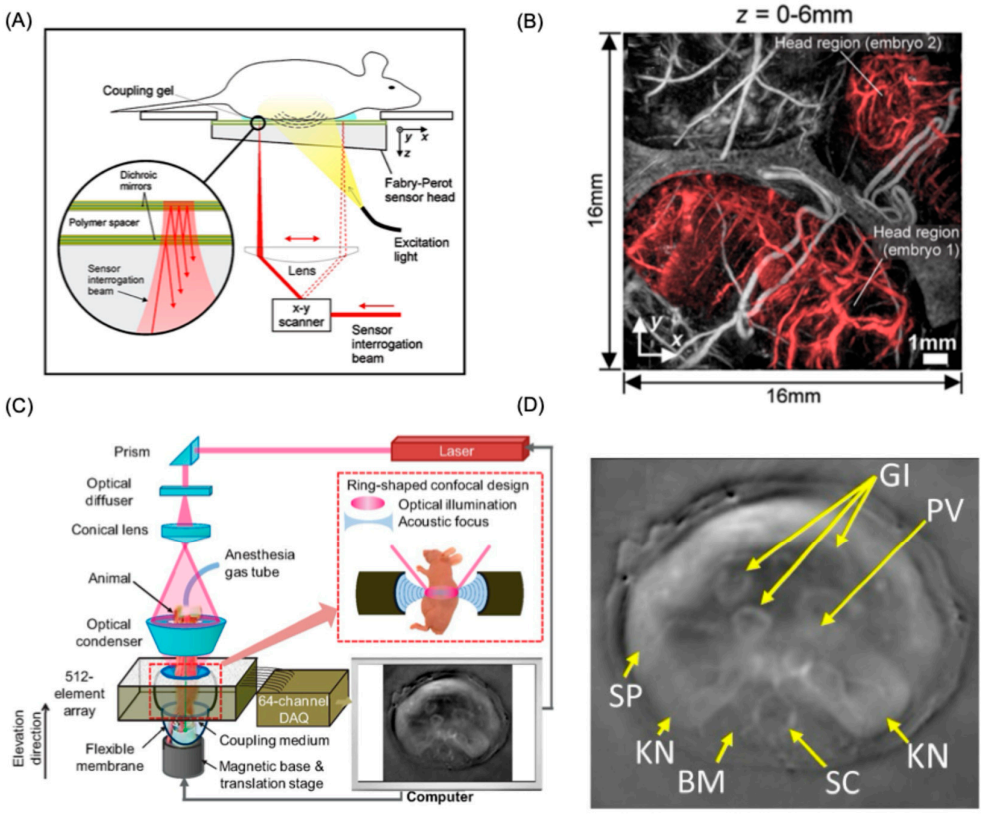

 doi:10.20944/preprints202603.1150.v1

Figure 3. Photoacoustic Computed Tomography Imaging system for in vivo applications. (A) Schematic representation of a Fabry–Perot interferometer–based photoacoustic computed tomography (PACT) system. Photoacoustic signals are generated following absorption of nanosecond pulses from a wavelength-tunable optical parametric oscillator (OPO) laser and are detected using a transparent polymer Fabry–Perot ultrasound sensor. The sensor consists of two dichroic mirror layers separated by an approximately 40 μm polymer spacer, forming the interferometric cavity. Acoustic waves are recorded by raster-scanning a continuous-wave (CW) focused interrogation laser across the sensor surface, where acoustically induced changes in cavity reflectivity are measured at each position to generate two-dimensional maps. (B) Maximum-amplitude projection of the reconstructed three-dimensional dataset (0–6 mm depth), highlighting two embryos (shown in red). Reproduced with permission from [48]. Copyright 2012, SPIE Digital Library. (C) Experimental configuration of a full-ring confocal whole-body photoacoustic computed tomography (RC-PACT) system. A schematic overview of the imaging setup is presented, with the dashed inset illustrating a cross-sectional view of the confocal geometry. (D) Representative in vivo RC-PACT images of athymic mice obtained noninvasively in the kidney region. Labeled anatomical structures include backbone muscle (BM), gastrointestinal tract (GI), kidney (KN), liver (LV), portal vein (PV), spinal cord (SC), and spleen (SP). Reproduced with permission from [49]. Copyright 2012, SPIE Digital Library. .

2.2.3. Endoscopic and Probe-Based PAI

Photoacoustic endoscopy (PAE) enables minimally invasive PAI by integrating optical excitation and acoustic detection within compact endoscopic probes [53,54]. This configuration allows localized visualization of tissue composition, vascular architecture, and functional biomarkers inside luminal organs, including the gastrointestinal and reproductive systems. When combined with ultrasound imaging, PAE provides complementary structural and functional information, supporting real-time guidance during endoscopic procedures. Early PAE platforms demonstrated intraluminal PAI but were limited by single-modality operation and slow acquisition speeds. Subsequent developments introduced dual- and multimodal probes incorporating photoacoustic, ultrasound, and fluorescence imaging, enabling three-dimensional visualization of vascular and luminal anatomy [55]. Continued probe miniaturization improved compatibility with standard endoscopic channels, advancing its translational potential[56].

Although PAE has been explored for many years as a clinical extension of PAI, several technical challenges have hindered its widespread clinical adoption [57]. Recent studies, however, demonstrate meaningful progress toward overcoming these barriers, particularly in probe design and light–acoustic integration. One of the primary challenges in multimodal PAE systems is achieving efficient, stable light delivery within the compact endoscopic geometries. To address this, Wen and co-workers developed a disposable photoacoustic–ultrasound (PAUS) endoscopic catheter coupled with a dedicated power interface, enabling switchable operation, internal three-dimensional scanning, and reproducible performance for gastrointestinal imaging [58]. By optimizing optical relay design, they significantly reduced waveguide insertion losses while maintaining high optical power delivery. Their focus-adjustable acousto-optic coaxial probe enabled high-sensitivity optical-resolution imaging, achieving real-time visualization of colonic microvasculature and tissue layering at micrometer-scale resolution in rats, highlighting its promise for the detection of gastrointestinal disease.

Complementary advances have focused on improving probe adaptability to the endoscopic environment. Zhu and colleagues introduced a hydrostatic balloon-based catheter incorporating a miniaturized ultrasound array and angled optical fiber, allowing conformal acoustic coupling along irregular intestinal surfaces [57]. This design enabled effective photoacoustic evaluation of inflammatory and fibrotic intestinal conditions and demonstrated sufficient penetration depth for in vivo differentiation of normal and pathological tissue states. Notably, the collapsible balloon configuration is compatible with conventional ileocolonoscopy, underscoring the translational potential of such PAE systems for clinical gastrointestinal diagnostics.

 doi:10.20944/preprints202603.1150.v1

The fundamental trade-offs between spatial resolution and penetration depth have led to two principal PAE modes: acoustic-resolution systems optimized for deeper imaging and optical-resolution systems that achieve higher lateral resolution at superficial depths[59]. Recent advances in scanning strategies, autofocusing mechanisms, and panoramic imaging geometries have improved imaging speed, resolution, and robustness. More recently, optical–scanning–based and Fabry–Pérot–based probes have enabled compact, high-resolution PAE systems with enhanced signal-to-noise ratios, facilitating in vivo assessment of vascular dynamics and tissue oxygenation [60]. Collectively, these developments position PAE as a promising tool for functional, image-guided endoscopic diagnostics.

3. Advantages of PAI Compared with Other Imaging Modalities

PAI is a hybrid modality that uniquely combines optical excitation with ultrasonic detection, thereby overcoming key limitations of conventional optical and clinical imaging techniques. Unlike traditional optical methods that rely on weakly penetrating ballistic photons, PAI detects ultrasound waves generated by optical absorption, allowing high-resolution imaging at depths far beyond the optical diffusion limit. Because acoustic waves scatter minimally in soft tissue, PAI preserves spatial resolution even at depths of several millimeters to centimeters beneath the surface.

PAI is inherently sensitive to optical absorption, making it exceptionally powerful for molecular and functional imaging[61]. By selecting excitation wavelengths matched to specific absorption spectra, PAI can differentiate a wide range of endogenous chromophores, including hemoglobin, melanin, lipids, and water, thereby enabling anatomical, functional, metabolic, and histological imaging without ionizing radiation. The use of exogenous absorbers, including organic dyes, nanoparticles, and genetically encoded probes, further enhances sensitivity and enables deep-tissue molecular imaging under clinically safe laser exposure limits.

Compared with established clinical modalities, PAI offers a unique balance of penetration depth, spatial resolution, and contrast[35,36]. MRI provides excellent soft tissue contrast but suffers from long acquisition times and limited temporal resolution. PET and SPECT enable high sensitivity but are constrained by poor spatial resolution and reliance on ionizing radiation, limiting longitudinal studies. X-ray CT similarly employs ionizing radiation and lacks molecular specificity, while conventional ultrasound imaging provides limited contrast beyond vascular structures [62,63]. PAI bridges these gaps by delivering high-resolution, noninvasive imaging with rich optical contrast at clinically relevant depths.

The advantages of PAI are increasingly supported by translational and early clinical investigations, particularly in oncology[35]. Studies using prototype PAI systems for breast imaging have demonstrated the ability to visualize tumor-associated vascular patterns and reduced hemoglobin oxygenation relative to surrounding healthy tissue, enabling differentiation between benign and malignant lesions and improved lesion delineation [64]. Multispectral imaging implementations have further enabled discrimination of sentinel lymph node metastases in melanoma by separating melanin-derived signals from hemoglobin absorption, addressing a major challenge in conventional nodal assessment. Beyond breast and melanoma applications, PAI-based analyses of hemoglobin oxygenation and lipid content have shown promise in distinguishing malignant from benign tissue in prostate, thyroid, and ovarian specimens [61,65]. Together, these findings underscore the growing potential of PAI as a complementary clinical imaging modality capable of noninvasive functional and molecular characterization of disease.

An additional advantage of PAI is its scalable resolution, which can be tuned by adjusting the detected acoustic frequency, enabling multiscale imaging from cellular and tissue levels to whole-organ and small-animal imaging using the same optical contrast mechanism [66]. This versatility has driven rapid advances in preclinical research and growing clinical translation, including functional brain imaging [67,68], whole-body small-animal imaging[69,70], human organ visualization[71,72], and emerging machine learning–assisted reconstruction techniques[73,74]. Overall, PAI represents a powerful complementary modality that uniquely integrates depth, resolution, and molecular

 doi:10.20944/preprints202603.1150.v1

specificity, positioning it as a transformative tool for biomedical research and future clinical applications. **Table 1** compares PAI with other imaging modalities in terms of resolution, sensitivity, and application.

4. Functional and Contrast-Enhanced PAI

Functional PAI exploits the intrinsic optical absorption of endogenous chromophores, including hemoglobin, lipids, and water, to noninvasively assess physiological and metabolic processes[26,75]. Multispectral acquisition allows quantitative mapping of parameters such as blood oxygen saturation, hemoglobin concentration, and hemodynamic changes, providing valuable insight into tissue perfusion, oxygen utilization, and organ function. In contrast, contrast-enhanced PAI employs exogenous photoabsorbing agents to further improve sensitivity and molecular specificity[76,77]. These agents, ranging from small organic dyes to engineered nanoparticles, are designed to generate strong photoacoustic signals, enabling visualization of weakly absorbing structures and targeted molecular events. Continued advances in contrast agent design are expanding the diagnostic and theranostic potential of PAI, supporting its growing role in biomedical imaging and precision medicine.

4.1. Endogenous Contrast Mechanisms

Several natural tissue components, including hemoglobin, melanin, lipids, collagen, elastin, and water, act as intrinsic optical absorbers and form the basis of this molecularly sensitive, label-free imaging strategy, which is well suited for rapid clinical translation (**Figure 4A**)[78]. These endogenous chromophores exhibit distinct absorption profiles across the near-infrared (NIR) window (approximately 700–1100 nm), allowing wavelength selection to optimize photoacoustic contrast from specific tissue constituents.

Hemoglobin serves as a highly effective intrinsic absorber for photoacoustic signal generation across the visible and near-infrared spectral regions[79]. Beyond structural visualization of blood vessels, PAI enables assessment of vascular function by exploiting wavelength-dependent optical properties of hemoglobin. In particular, the relative concentrations of oxygenated (HbO_2) and deoxygenated hemoglobin (Hb) can be quantified, as oxygen binding induces characteristic alterations in hemoglobin's absorption spectrum[80,81]. By acquiring photoacoustic signals at multiple visible and near-infrared wavelengths, it is possible to estimate blood oxygen saturation and

Table 1. A comparison of various imaging modalities with PAI.

Modality	Spatial Resolution	Imaging Depth	Contrast Agents	Primary Functional Parameters	Major Advantages	Main Limitations
NIR-II Imaging	System-dependent (mm–cm scale)	Several mm to cm	Organic fluorophores, inorganic nanoparticles	Vascular morphology, hemodynamics	High spatial resolution, deep tissue penetration, real-time imaging	Contrast agent risks, high equipment cost
PET	4–6 mm	Whole body	^{18}F-FDG, ^{18}F-NaF	Standardized uptake value (SUV), metabolic rate, perfusion	Whole-body imaging, high sensitivity, quantitative metabolic	Radiation exposure, limited spatial resolution, high cost

 doi:10.20944/preprints202603.1150.v1

					information	
MRI	0.3–1 mm	Whole body	Gadolinium-based agents	Degree of stenosis, hemodynamics	Non-invasive, radiation-free, high soft tissue contrast	Long scan time, contrast-related risks, limited microvascular detail
CT	0.2–1 mm	Whole body	Iodinated contrast agents	Degree of stenosis, vessel wall characteristics	High spatial resolution, rapid 3D imaging	Ionizing radiation, nephrotoxicity risk, limited subtle pathology detection
US	Tens of μm to several mm	Up to several cm	Typically, none (optional microbubbles)	Vascular morphology, blood flow	Real-time, radiation-free, low cost	Operator-dependent, resolution-depth tradeoff
PAI	Tens to hundreds of μm	Several mm to cm	Endogenous (Hb, melanin, lipid) and exogenous (dyes, nanoparticles)	Oxygen saturation, hemoglobin concentration, vascular morphology, metabolic rate	Combines optical contrast with ultrasound resolution, functional + structural imaging	Limited deep penetration, ongoing clinical standardization

distinguish oxygen-rich from oxygen-poor regions within tissues. This capability allows real-time, in vivo mapping of both vascular architecture and oxygenation status, providing valuable insights into a wide range of physiological and pathological conditions. Photoacoustic assessment of hemoglobin oxygenation has been applied to the study of tumor hypoxia[82], tissue regeneration during wound healing[83], ischemic injury such as stroke[84], impaired placental oxygen delivery[81], and functional processes within the brain[85]. Together, these applications highlight the versatility of hemoglobin-based photoacoustic contrast for diagnosing disease and monitoring dynamic biological processes.

Representative demonstrations of blood-derived contrast in PAI are illustrated in **Figure 4**. One example shows a depth-resolved maximum-intensity projection of vascular networks in the human palm acquired at 795 nm, where color mapping indicates vessel depth (**Figure 4A**)[86]. This image reveals clear stratification of the vascular anatomy, with major arterial structures such as the superficial palmar arch and digital arteries positioned deeper within the tissue than the superficial venous network. In addition to structural visualization, PAI supports functional assessment of tissue physiology. As shown in **Figure 4B**, wavelength-dependent imaging enables mapping of blood oxygen saturation within the somatosensory cortex during electrically evoked neural activity, allowing simultaneous observation of microvascular architecture and dynamic oxygenation changes

 doi:10.20944/preprints202603.1150.v1

[87]. This ability to image both normal and pathological vasculature underlies the value of PAI in cancer detection, particularly in breast tissue. An example of whole-breast vascular imaging is presented in **Figure 4C**, where depth-encoded visualization provides three-dimensional insight into vascular distribution throughout the tissue, offering a comprehensive view of breast vasculature relevant for diagnostic evaluation[88].

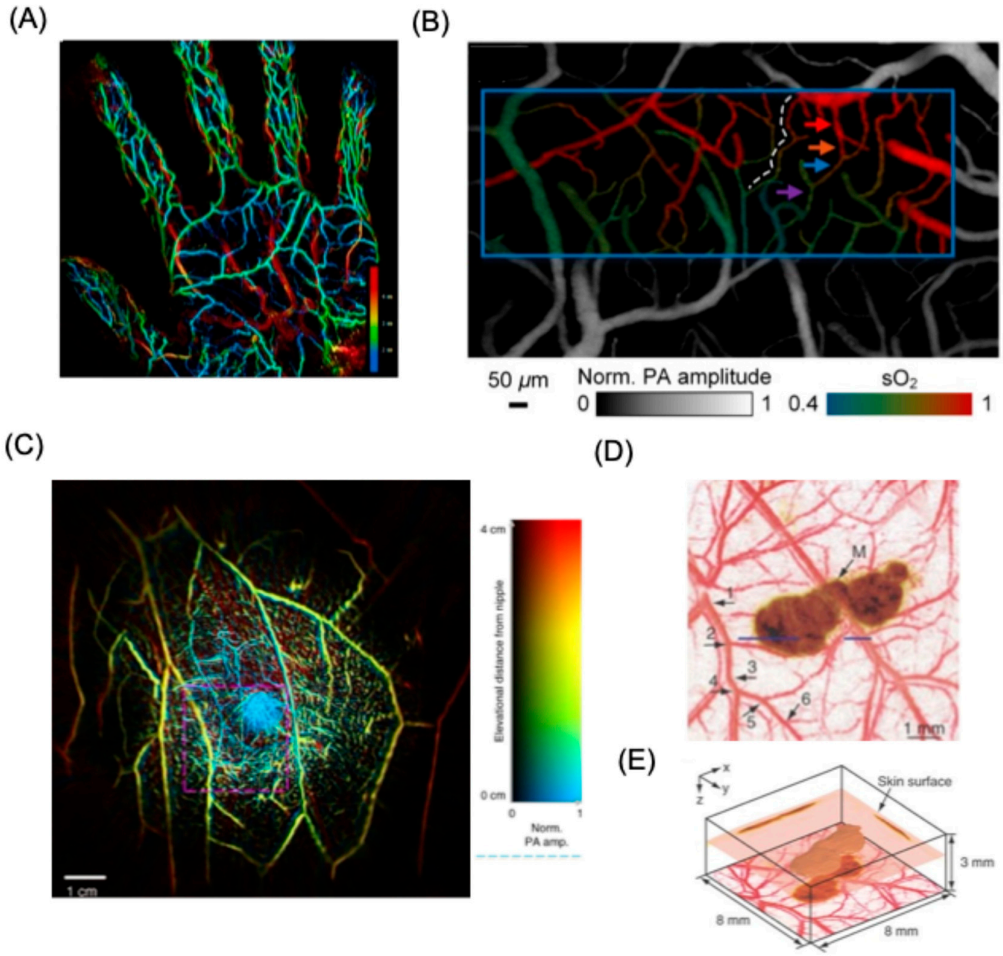

Figure 4. Endogenous contrast-based PAI application. (A) Maximum-intensity projection photoacoustic (PA) image showing the vascular network of the palm acquired at 795 nm, where the color scale indicates imaging depth. Reproduced with permission from [86], Copyright 2018, Nature Publishing group. (B) Photoacoustic oxygen saturation map of the somatosensory cortex recorded during electrical stimulation. The blue box highlights the selected region of interest used for subsequent functional imaging analysis. Reproduced with permission from[87]. Copyright 2020, SPIE. (C) Photoacoustic computed tomography image illustrating the vascular architecture of the right breast in a healthy female volunteer, with depth information represented using a color-coded scale. Reproduced with permission from [88]. Copyright 2018, Nature Publishing group. (D) Composite maximum-amplitude projection (MAP) images obtained by projecting the maximum photoacoustic signals along the z-axis. Blood vessels (584 nm) are pseudo-colored red, and melanoma (764 nm) is pseudo-colored brown. Six hierarchical levels of vascular branching (1–6) are visible. (E) Three-dimensional reconstruction of the melanoma from 764 nm data. MAP images projected along the x- and y-axes are shown on the side walls, and the composite image from D is displayed at the bottom. The tumor surface is located 0.32 mm below the skin, with a thickness of 0.3 mm. Reproduced with permission from [89]. Copyright 2006, Nature Publishing group.

The strong hemoglobin contrast also makes PAI exceptionally powerful for characterizing vascular structure and function across different spatial scales[90]. From resolving microvascular

 doi:10.20944/preprints202603.1150.v1

networks to assessing larger vessel architecture, PAI provides scalable resolution at depths beyond the reach of purely optical techniques. This capability has been widely applied to study vascular remodeling in tumors, where abnormal vessel organization and hypoxia are hallmarks of disease progression, as well as in metabolic disorders such as diabetes, where micro- and macrovascular dysfunction play a central role[35,42]. In addition, PAI has demonstrated promise in imaging specialized vascular beds, including lymph nodes and chorioretinal tissues, highlighting its potential for both basic biological discovery and future clinical translation in vascular diseases[91].

Melanin also produces intense photoacoustic signals and has been successfully explored for melanoma detection [92]. Melanin has a broad absorption spectrum that spans from visible light to near infrared region (NIR) wavelengths (400-1064 nm) and thus allows for a wide range of excitation wavelengths to be used in PAI. Melanin present in ocular tissues such as the uvea and is highly concentrated in pigmented tumors, including ocular melanoma[93]. PAI studies have shown that melanin generates stronger signals at shorter wavelengths (e.g., 532 nm) compared to longer wavelengths (e.g., 1064 nm), reflecting its wavelength-dependent absorption, while longer wavelengths provide greater imaging depth [79]. High-resolution photoacoustic microscopy has further enabled differentiation between retinal pigment epithelium and choroidal melanin, aided by optical modeling approaches to optimize spatial resolution [94,95]. Beyond ocular applications, photoacoustic detection of melanin has been explored for identifying circulating melanoma cells, offering potential benefits for melanoma diagnosis and treatment monitoring [96]. While near-infrared wavelengths can enhance contrast between melanin and hemoglobin, limited penetration depth restricts detection of thicker or deeply located lesions. Spectral overlap between melanin and blood remains a challenge, though advanced spectral analysis and three-dimensional image reconstruction approaches have improved sensitivity and enabled visualization of small melanoma features that are difficult to resolve using conventional two-dimensional imaging. Langhout and co-workers advanced spectral photoacoustic analysis by systematically evaluating the absorption signatures of multiple chromophores across the 680–970 nm range [97]. While this approach enabled differentiation between hemoglobin and melanin, detection of small melanoma lesions remained challenging due to insufficient photoacoustic signal intensity, resulting in poor agreement with the expected spectral signature. This limitation was later addressed by Zhang and colleagues, who employed depth-resolved reconstruction of photoacoustic z-stacks acquired at 764 nm to generate three-dimensional morphological representations (**Figure 4D**) [89]. The resulting volumetric imaging strategy improved feature visibility and allowed identification of melanoma structures that were not discernible using conventional two-dimensional PAI (**Figure 4E**).

In contrast, although lipids, collagen, elastin, and water can contribute to endogenous photoacoustic contrast and are valuable in other biological contexts, their relevance in oncology remains limited[79] . Their comparatively weaker absorption in the near-infrared region and lower signal-to-noise ratios reduce their reliability for robust tumor visualization when compared with hemoglobin-based contrast.

4.2. Exogenous and Functional Enhancement Strategies

Endogenous photoacoustic contrast is inherently constrained by the narrow optical absorption range of native biomolecules, limiting both imaging depth and molecular specificity. In contrast, recent advances in the design of organic dyes and nanomaterials with tunable absorption spanning the NIR-I and NIR-II windows have significantly expanded the capabilities of PAI [75,98]. These exogenous contrast agents can be engineered to exhibit red-shifted absorption profiles that minimize interference from intrinsic chromophores, enabling deeper tissue penetration and more selective visualization of cellular and molecular processes beyond conventional anatomical and functional imaging. An effective exogenous photoacoustic probe must combine strong, spectrally distinct signal generation with molecular or cellular targeting capability. Typically, such agents comprise a signal-producing core coupled to a targeting moiety, with the mode of assembly dictated by their chemical properties and stability. Simple surface-conjugation strategies are commonly employed for inorganic

 doi:10.20944/preprints202603.1150.v1

nanostructures, whereas hydrophobic small-molecule dyes are frequently incorporated into polymer-based carriers to confer aqueous solubility and biological targeting [99]. **Table 2** represents a range of exogenous contrast agents used for the PAI for various disease.

Table 2. List of various exogenous contrast agents for PAI.

Exogenous Contrast agents	Size	Absorption (nm)	Application	Ref
Small organic contrast agents				
Indocyanine green	~ 2 nm	810	In vivo mouse imaging	[100,101]
BSA-Cerium-ICG	28 nm	790	Endometriosis detection	[102]
Methylene blue	~2 nm	650–700	In vivo imaging for sentinel lymph node; Monitoring of drug release	[103,104]
Evans Blue	<2 nm	610	In vivo capillary imaging. in vivo mouse brain imaging	[105,106]
Phthalocyanine	<2 nm	759	DNA-based nanosensor for interferon Gamma detection	[107]
NIRb14 Dye	<2 nm	800	In vivo imaging for 4T1 tumor-bearing mice; PTT for 4T1 tumor-bearing mice	[108]
BODIPY-Xanthene Hybrids	Not reported	700–1000 nm	Intestinal and whole-body vasculature	[109]
Perylene Diimide NPs	70 nm 48 nm	400–800 nm 700 nm	In vitro PAI Brain tumor imaging	[110,111]
Inorganic Nanoparticles				
Gold nanorod	Aspect ratio: 2	700 nm	Imaging of inflammatory response	[112,113]
Gold nanorod	L: 52.75 nm W: 20.71 nm	780 nm	Endometriosis detection and PTT	[16]
Miniature gold nanorod	L49nm W: 8 nm	1000–1700 nm	Molecular imaging of tumor targeting via gastrin-releasing peptide receptor	[114]
Gold sphere	20 nm	700–780 nm	Intravascular imaging of macrophages	[115,116]
Gold-Silver hybrid nanorods	W: 12–14 nm L: 50–55 nm	530, 800 nm	Monitoring silver release for antibacterial treatment	[117]

 doi:10.20944/preprints202603.1150.v1

	Thickness: 10 nm			
Prussian blue	L: Small: 20 nm Medium: 40 nm. Large: 170 nm	700 nm	In vivo imaging of mouse abdomen upon subcutaneous injection of PBNCs in Matrigel	[118,119]
Exosome-Prussian blue	~70 nm	700–750 nm	In vivo brain tumor imaging and PTT	[67]
Gold nanostar	35 nm	700–900 nm	In vivo tumor imaging	[120]

Where W: Width, L: Length for nanoparticles.

4.2.1. Nanoparticles as Exogenous Contrast Agents

Among various exogenous contrasting agents, gold nanoparticles (AuNPs) are a promising candidate owing to tunable optical absorption, surface chemistry modification and excellent photothermal conversion efficiencies[116,121]. Since the discovery of local surface plasmon resonance depends on the AuNPs geometry, a myriad of gold nanostructures, including gold nanorods (AuNRs), gold nanocages (AuNCs), gold nanoshells (AuNShs), and gold nanostars (AuNSts) had been synthesized, offering tunable optical windows from 530 to beyond 1000 nm depending on their anisotropic structure [116].

Among AuNPs, gold nanorods (AuNRs) are among the most widely investigated exogenous photoacoustic contrast agents due to their straightforward synthesis and the ability to precisely tune their optical absorption into the near-infrared region by controlling aspect ratio[114,122]. Chen and co-workers reported the development of ultrasmall AuNRs [(8 ± 2) nm × (49 ± 8) nm] with dimensions significantly reduced relative to conventional AuNRs, yet maintaining comparable aspect ratios (**Figure 5A**)[114]. These miniaturized structures exhibited absorption extending into the NIR-II window (1000–1700 nm) and produced markedly stronger photoacoustic signals than their larger counterparts. Modeling studies attributed this enhancement to a size-dependent increase in surface-to-volume ratio, revealing a quadratic dependence of photoacoustic amplitude on this parameter when optical absorption is normalized across nanorods of different sizes. In vivo experiments demonstrated a 4.5-fold increase in PA signal within tumor tissues following AuNR administration, underscoring the influence of structural properties of nanorods on their optical absorption behavior. Comparative analysis of small and large AuNRs in tumor-bearing mice revealed that both nanoparticles achieved tumor targeting when conjugated with GRPR-binding peptides and Cy5 dyes. After 24 hours, non-targeted large AuNRs produced stronger PA signals than smaller counterparts, likely due to tumor heterogeneity (**Figure 5B (i-ii)**). In contrast, targeted small AuNRs generated higher PA signal intensity compared to larger targeted nanorods, emphasizing the critical role of nanoparticle size in optimizing targeting efficiency and PA imaging performance (**Figure 5B(iii-iv)**). Despite improved tumor retention, comparable accumulation in clearance organs such as the liver, kidney, and spleen was observed, reflecting limitations associated with reticuloendothelial system uptake.

Beyond tumor imaging, AuNRs have been applied in several vascular and inflammatory imaging contexts [112,115]. Their use as tracers for sentinel lymph node mapping has demonstrated improved imaging depth and contrast relative to spherical gold nanoparticles. Targeted AuNRs and gold nanoshells (AuNShs) functionalized against endothelial inflammatory markers, such as ICAM-1, have enabled intravascular PAI of atherosclerotic lesions and vascular inflammation in preclinical

 doi:10.20944/preprints202603.1150.v1

models. In addition, polyethylene glycol–modified hollow AuNShs and nanocages (AuNCs) have been employed for cerebral vasculature imaging following systemic administration, yielding significantly enhanced vessel visibility compared to endogenous contrast alone[115].

Recent developments have further expanded the functionality of gold-based probes. Gas-generating AuNPs have been engineered to amplify both ultrasound and photoacoustic signals through laser-triggered nitrogen release, achieved by conjugating azide-containing compounds onto polymer-coated gold surfaces[123]. Upon near-infrared excitation, these nanoparticles act as photocatalysts, generating nitrogen gas that enhances acoustic contrast. Collectively, gold nanoparticles remain attractive photoacoustic probes owing to their tunable surface plasmon resonance and well-established gold–thiol chemistry for biomolecular conjugation. However, challenges remain in achieving robust, scalable synthesis for complex morphologies and ensuring thermal stability during laser irradiation, often necessitating additional surface modifications such as silica encapsulation. Furthermore, comprehensive long-term studies are still required to fully assess the biological fate and potential toxicity associated with gold nanoparticle accumulation in vivo.

AuNRs with a longitudinal absorption peak near 760 nm enabled contrast-enhanced PAI of ovarian cancer, allowing clear visualization of MDA-435S xenograft tumors in vivo[124]. To further amplify photoacoustic output, gold nanoparticles were assembled into chain-like vesicular structures using block copolymer templates. These chain vesicles exhibited enhanced optical absorption, generating strong photoacoustic signals at 780 nm and producing an approximately eightfold signal increase compared with non-assembled gold nanoparticles following subcutaneous administration in mice (**Figure 5C**)[125]. Surface-engineered AuNPs have also enabled activatable photoacoustic contrast mechanisms. Ag-AuNR hybrid nanoparticles were designed with a silver shell that suppressed the photoacoustic signal originating from the AuNR core (**Figure 5D**) [117]. Upon exposure to ferricyanide, the silver layer was selectively removed, releasing silver ions and unmasking the photoacoustic signal from the underlying AuNRs. This activation produced strong photoacoustic contrast at 750 nm while simultaneously delivering potent antibacterial activity exceeding 99.99%. In vivo PAI before and after silver etching confirmed real-time silver ion release through marked changes in photoacoustic signal intensity (**Figure 5E**).

Silver nanostructures have also been explored as plasmonic contrast agents for PAI due to their strong localized surface plasmon resonance and morphology-dependent optical properties. Compared with gold-based nanoparticles, silver exhibits sharper plasmon bands and approximately 10% higher optical absorption, resulting in enhanced photoacoustic signal generation. At the same time, Ag presents important limitations, primarily due to its higher chemical reactivity relative to Au, which can affect colloidal stability and biological compatibility. To combine the stronger plasmonic performance of Ag with the chemical inertness of Au, Lee and colleagues developed porous Ag–Au alloy nanoparticles (pAgAuNPs). In whole-body in vivo mouse imaging, these porous alloyed particles generated substantially higher photoacoustic signals than standard AuNPs, with reported enhancements of approximately 2.7-fold. Beyond Ag–Au alloy systems, other noble-metal pairings, including Pt–Ag and Pd–Pt configurations, have also been explored to fabricate plasmonic architectures with tunable optical properties.

 doi:10.20944/preprints202603.1150.v1

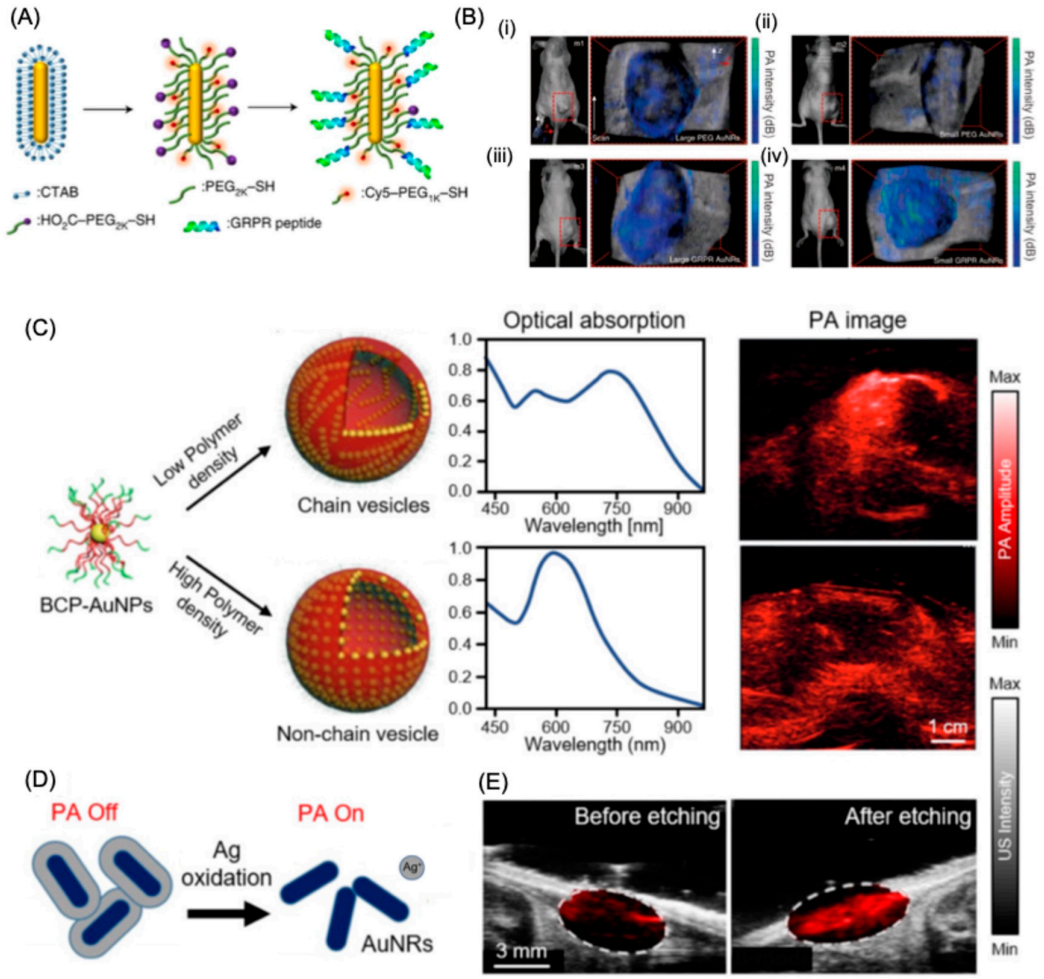

Figure 5. Gold nanoparticle based exogenous contrasting agents for PAI. (A) Schematic representation and (B) representative photographs of photoacoustic (PA) imaging in tumor-bearing mice (m1–m4) following administration of large and small AuNR formulations. Panels (i, ii) show PA images of non-targeted large and small AuNRs, respectively, while panels (iii, iv) display PA images of GRPR-targeted large and small AuNRs. The color-coded PA signal maps are superimposed onto corresponding ultrasound images to provide anatomical context. Reproduced with permission from [114]. Copyright 2019, Nature publishing group. (C) Schematic depiction of the preparation of BCP-AuNP vesicles, along with their optical absorption characteristics and contrast-enhanced photoacoustic (PA) images. Reproduced with permission from [125]. Copyright 2015, Wiley Publishers. (D) Illustration of the photoacoustic signal modulation in the presence and absence of a silver (Ag) coating. (E) Combined PA and ultrasound (US) images acquired before and after silver etching. Abbreviations: PA, photoacoustic; US, ultrasound; BCP, block copolymer; AuNP, gold nanoparticle; AuNR, gold nanorod; Ag, silver. Reproduced with permission from[117]. Copyright 2018, American Chemical Society.

Beyond metal nanoparticles, inorganic dye–based nanomaterials such as Prussian blue nanoparticles (PBNPs) have emerged as versatile platforms for multimodal photoacoustic contrast [67,118]. A key advantage of Prussian blue lies in its long history of clinical use and established FDA approval, underscoring its favorable biocompatibility profile. PBNPs are known for its strong photothermal therapy applications[119]. Building on this concept, size-controlled photomagnetic Prussian blue nanocubes have been synthesized by Dumani et al. using superparamagnetic iron oxide nanoparticles as sacrificial templates [118]. These nanocubes exhibit strong magnetic responses along with pronounced optical absorption near 700 nm, enabling their use as stable, dual-function

 doi:10.20944/preprints202603.1150.v1

contrast agents for both magnetic resonance imaging and photoacoustic tomography in vivo. Meghan and colleagues recently reported the development of PBNPs coated with exosomes derived from U-87 glioblastoma cells as a targeted diagnostic platform for PAI of glioblastoma [67]. Owing to their high photothermal conversion efficiency, these exosome-coated nanoparticles were also evaluated for photothermal therapy, resulting in approximately 50% tumor growth inhibition in both in vitro and in vivo models. PAI studies further demonstrated the superior tumor-targeting capability of the exosome-coated PBNPs compared with PEGylated and RGD-functionalized counterparts.

4.2.2. Carbon Nanotube as Exogenous Contrast Agent

Carbon nanotubes (CNTs) have emerged as promising exogenous contrast agents for PAI owing to their strong and broadband optical absorption in the visible and near-infrared regions, which enables high-contrast imaging with improved penetration depth and spatial resolution[126–128]. Single-walled carbon nanotubes (SWNTs) generate robust photoacoustic signals even at low laser fluence due to efficient NIR light absorption and thermal confinement[127,129]. Their photoacoustic performance can be dramatically enhanced through molecular functionalization; for example, conjugation with indocyanine green (ICG) increases optical absorbance by up to 20-fold at ~780 nm and yields a ~300-fold improvement in detection sensitivity compared with unmodified SWNTs in vivo imaging study [127]. At this wavelength, background tissue absorption is minimal, further improving signal-to-noise ratios. Notably, ICG exhibits optical absorption efficiencies approximately 7-fold higher than SWNTs and ~8500-fold higher than commercial gold nanorods on a per-weight basis, underscoring the strong photoacoustic sensitization achieved through SWNT–ICG hybrid systems.

Beyond signal enhancement, CNTs offer substantial versatility for targeted, multimodal, and theranostic photoacoustic applications [126]. Gold-plated CNTs, or golden carbon nanotubes (GNTs), integrate the plasmonic properties of gold with the lightweight, hollow cylindrical structure of CNTs, resulting in exceptionally high NIR contrast (up to ~102-fold enhancement), efficient photothermal conversion, and low material dose requirements [130]. These properties have enabled combined photoacoustic and photothermal tumor imaging and ablation with minimal observed toxicity in preliminary studies. CNTs can also be functionalized for molecular targeting, as demonstrated by RGD-conjugated SWNTs that selectively bind $\alpha v\beta 3$ integrins and increase tumor photoacoustic signal by 8-fold in glioma xenograft models [127]. Antibody [131], hypoxia[132], and inflammation-targeted CNTs have further enabled sensitive imaging of early tumors [133], atherosclerotic plaques[134], and disease-associated immune cell infiltration [135] using PAI. In addition to oncology, CNT-based agents have been applied to vascular and lymphatic mapping, including sentinel lymph node imaging. They can act as nanoscale photoacoustic emitters capable of generating high-frequency, broadband ultrasound for imaging, drug delivery, and gene transfection[130,136]. Collectively, these studies highlight CNTs as multifunctional PAI platforms that combine high sensitivity, molecular specificity, and therapeutic potential.

4.3. Organic Dyes as Exogenous Contrast Agents

Organic dyes, which can absorb light in NIR-I and NIR-II, are widely used as exogenous contrast agents for PAI and for various biomedical applications[98,137,138]. FDA-approved dyes such as methylene blue (MB), Evans blue (EB), and indocyanine green (ICG) are widely used as PA contrast agents that absorb light in NIR region I. Dyes with moderate to low fluorescent quantum yields poses high thermal conversion efficiencies which in turn enhance the PA signal intensity.

4.3.1. Organic Dyes as Contrast Agents with Low NIR Absorption (650–800 nm)

Small-molecule optical dyes have been among the earliest and most widely used contrast agents for lymphatic PAI due to their strong absorption in the visible and near-infrared regions of the spectrum. In rat models, local forepaw injection of MB enabled clear visualization of sentinel lymph

 doi:10.20944/preprints202603.1150.v1

nodes (SLNs), yielding approximately a twofold increase in photoacoustic signal intensity relative to control images when excited at 635 nm[139]. Comparable signal enhancement (~2×) was also observed in SLNs following administration of EB, indicating that blue dyes with high visible absorption can effectively accumulate in lymphatic structures and generate measurable photoacoustic contrast[140]. Beyond free-dye solutions, stimulus-responsive contrast formulations have been developed to enable functional control over photoacoustic signal generation. Dye-loaded microbubbles containing MB were engineered to support combined photoacoustic and ultrasound imaging, with both modalities exhibiting signal changes that scaled with microbubble concentration[141]. Importantly, exposure to high-intensity ultrasound pulses induced microbubble rupture, resulting in a pronounced 2.5-fold increase in photoacoustic signal output. This acoustically triggered enhancement demonstrates the feasibility of externally controlled contrast activation, enabling dynamic modulation of photoacoustic signals for biomedical investigations.

In addition to visible-absorbing dyes, near-infrared chromophores such as indocyanine green (ICG) have become central to contrast-enhanced PAI owing to their strong absorption in the first near-infrared window and favorable tissue penetration depth[142,143]. ICG-based imaging enabled clear delineation of lymphatic vessels from the surrounding blood vasculature in rat models, achieving photoacoustic signal enhancements of approximately 4.3-fold[144]. Notably, the higher fluorescence quantum yield of ICG compared with methylene blue and Evans blue allows simultaneous acquisition of fluorescence signals from SLNs. This property has been exploited for dual-modal photoacoustic and fluorescence imaging, as demonstrated in organ-specific applications such as bladder imaging following systemic or local ICG administration.

Beyond static contrast enhancement, organic nanostructures have enabled PAI of dynamic biological responses through activatable and environment-sensitive designs. A pH-responsive nanoprobe based on a semiconducting oligomer (SO) conjugated with a boron-dipyrromethene dye exhibited distinct PA responses as a function of local pH (**Figure 6A-B**) [145]. When administered to HeLa xenograft tumors in mice, the SO nanoprobes generated tumor-specific PA contrast due to the acidic tumor microenvironment, as revealed by differential signals at excitation wavelengths of 680 and 750 nm in a ratiometric way (**Figure 6C-D**). Activatable probes have also been developed to detect specific biochemical mediators using PAI. Nitric oxide (NO)–responsive nanoprobes exhibited a characteristic optical absorption shift from 770 nm to 680 nm upon NO interaction (**Figure 6E**)[146]. Multispectral PAI before and after nanoprobe administration in a lipopolysaccharide (LPS)-induced inflammation mouse model confirmed probe activation, producing a significant PA signal enhancement relative to controls (**Figure 6F**). Such approaches enable in vivo spatial mapping of NO levels, providing insight into inflammatory signaling and tumor-associated pathophysiology.

4.3.2. Organic Dyes as Contrast Agents with High NIR Absorption (800-900 nm)

Naphthalocyanine-based agents have emerged as promising NIR chromophores, with tunable absorption typically spanning the 800–1000 nm range [147]. Pioneering work by Zhang and co-workers demonstrated the feasibility of naphthalocyanines as in vivo photoacoustic contrast agents for imaging the gastrointestinal tract in mice [148]. Subsequently, a library of naphthalocyanine derivatives with precisely tunable optical windows was developed and employed as multicolor contrast agents for PAI of lymphatic networks in rats. In one representative study, two derivatives with absorption maxima at 707 nm and 860 nm were independently injected into the left and right forepaws of mice, enabling dual-color PAI that successfully delineated the lymphatic drainage pathways on each side [149]. Beyond lymphatic imaging, naphthalocyanines formulated into nanostructures have been applied for PAI of 4T1 breast tumors and for photothermal therapy[150]. In addition, naphthalocyanine-loaded nanodroplets have been explored for high-intensity focused ultrasound (HIFU)-mediated tumor ablation, with treatment monitored by combined photoacoustic and ultrasound imaging [151]. Naphthalocyanine dyes were encapsulated within perfluorohexane to create nanodroplets optimized for effective HIFU ablation. The resulting formulation exhibited a strong optical absorption maximum at 850 nm, and its in vivo imaging performance was validated

 doi:10.20944/preprints202603.1150.v1

following intravenous administration. Contrast-enhanced photoacoustic images were successfully obtained from MDA-MB-435S xenograft tumor regions in mice. Beyond imaging, the therapeutic efficacy of HIFU ablation was systematically evaluated, demonstrating enhanced treatment outcomes when guided by photoacoustic contrast. In vivo PA/US-guided HIFU studies revealed that these nanodroplets enhanced cavitation effects, promoted tumor cell necrosis and apoptosis, and significantly suppressed tumor growth for up to 12 days.

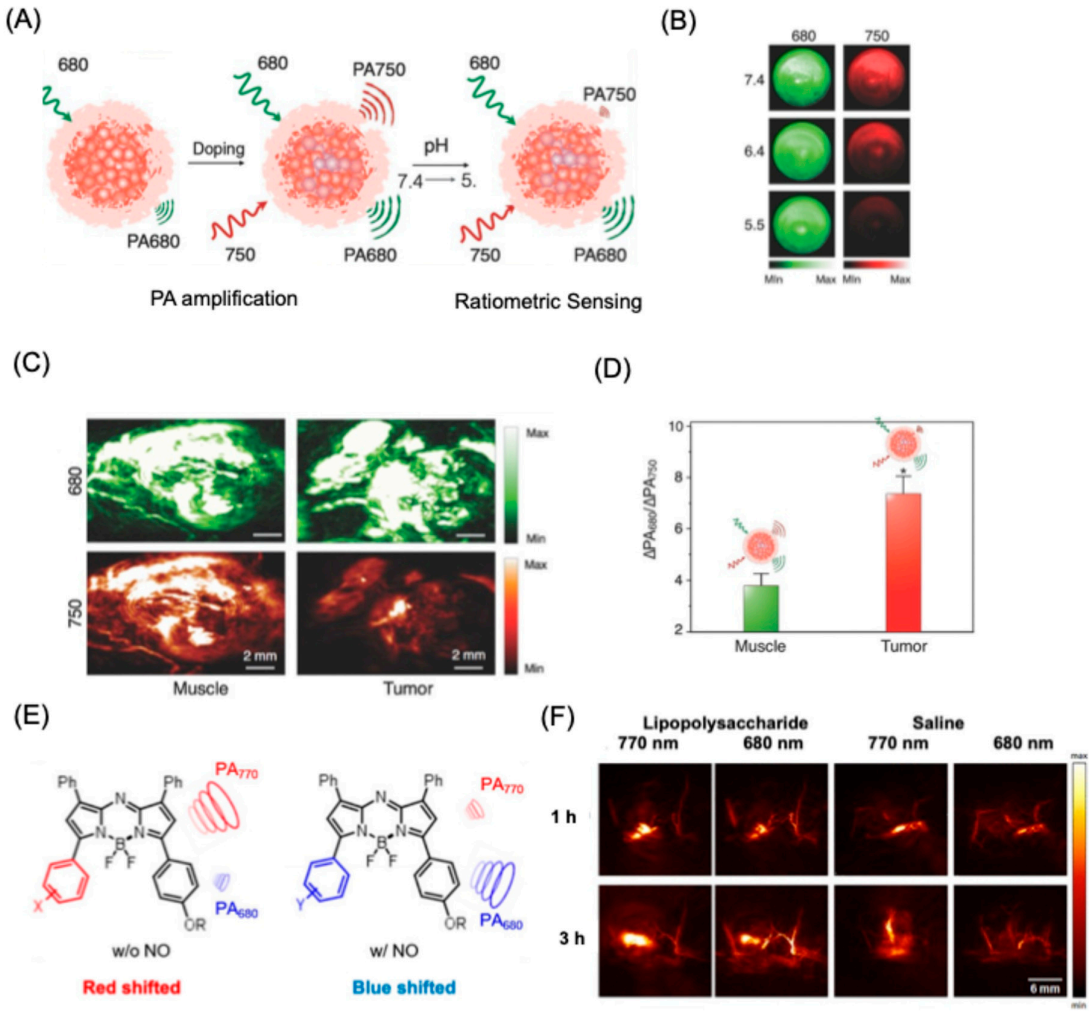

Figure 6. Ratiometric PAI using organic dyes. (A) Schematic illustration of the doping-induced photoacoustic (PA) signal amplification and the underlying pH-sensing mechanism. (B) PA images of the SON50 solution at different pH conditions (7.4, 6.4, and 5.5). Ratiometric imaging was performed using a pulsed laser tuned to 680 nm and 750 nm. (C) PA images and (D) corresponding ratiometric signals ($\Delta PA_{680}/\Delta PA_{750}$) obtained from muscle and tumor tissues following local administration of SON50 (10 μL, 10 μg mL^{-1}). Representative PA maximum intensity projection (MIP) images in the coronal view are shown. Reproduced with permission from [145]. Copyright 2016, Wiley Publishers. (E) Schematic for the signal switching for an NO- activated PA Probe. (F) Representative photoacoustic (PA) images demonstrating the response of APNO-5 to endogenous nitric oxide (NO) in a murine LPS-induced inflammation model. PA images were obtained from the mouse flank after subcutaneous administration of LPS or saline, followed by injection of APNO-5 (68 μg kg^{-1}). APNO-5 and its transformed product (tAPNO-5) were selectively imaged at 770 nm and 680 nm, respectively. Reproduced with permission from [146]. Copyright 2018, American Chemical Society.

 doi:10.20944/preprints202603.1150.v1

4.3.3. Organic Dyes as Contrast Agents with High NIR Absorption (>1000 nm)

Semiconducting polymeric nanoparticles (SPNs) and their polymeric counterparts can be used for NIR-II imaging applications owing to their combination of donor-acceptor moieties in the backbones. Jiang et al. fabricated SPNs with one donor and two acceptors, and this special structure allowed an optical absorption window at 750 and 1100 nm for the material (**Figure 7A**) [152]. PAI under NIR-I (750 nm) and NIR-II (1064 nm) excitation was evaluated in rat brain models following intravenous administration of the SPNs (**Figure 7B**). Notably, NIR-II excitation produced a 1.5-fold enhancement in signal-to-noise ratio compared with NIR-I excitation, highlighting the advantages of longer-wavelength excitation for deep-tissue imaging. In a related study, a metabolizable SPN formulation was developed that degrades into ultrasmall (~1 nm) fragments readily cleared by phagocytic pathways[153]. This SPN exhibited strong absorption near 1079 nm, enabling contrast-enhanced PA imaging at 1064 nm excitation. Using this platform, deep transcranial PA imaging was achieved with high signal fidelity, yielding signal-to-noise ratios of 4.6 for tumor regions and 2.3 for vascular structures.

Zhang et al. reported metabolizable SPNs with strong absorption extending from ~1079 nm to ~1300 nm, which generated significantly enhanced photoacoustic contrast following systemic administration in 4T1 tumor–bearing mice, yielding approximately twofold signal enhancement and enabling deep transcranial imaging with high signal-to-noise ratios for both tumor and vascular structures (**Figure 7C-D**) [154]. Building on this design strategy, Guo et al. developed an alternative two-acceptor SPN formulation optimized for 1064 nm excitation, achieving high-resolution PAI of the cerebral cortex vasculature with a signal-to-noise ratio of 22.3 at depths approaching 1 mm through the intact skull[155]. Collectively, these studies highlight the versatility of two-acceptor SPN architectures for wavelength-tunable, deep-tissue PAI with improved sensitivity and penetration depth.

5. Dynamic Contrast-Enhanced PAI (DCE-PAI)

Dynamic contrast-enhanced (DCE) PAI combines DCE imaging with PAI, which tracks the contrast agent uptake using light and ultrasound. This technique offers non-invasive detection of various disease models, tissue vascularity, perfusion, etc. Yang et al. used this technique for chronic wound curing and vascular perfusion studies [156].. OE-PAI was performed at different time points (days 0, 3, 6, and 9). Immediately following wound formation, levels of oxyhemoglobin (HbO_2), deoxyhemoglobin (Hb), total hemoglobin (HbT), and blood oxygen saturation (sO_2) are higher than in wounded tissue, reflecting increased local blood content and oxygenation. By day 3, these metrics declined markedly, preceding the measurable reduction in wound size observed at day 6. A continued downward trend was observed through days 6 and 9, although values remained above baseline, consistent with incomplete wound resolution at the final time point. Comparable temporal patterns were observed under both normoxic and hyperoxic breathing conditions, except for oxygen saturation at day 3 during hyperoxic exposure. DCE-PAI revealed slow ICG clearance immediately after wounding (day 0), followed by progressively faster wash-out on days 3, 6, and 9, consistent with advancing wound healing. Quantitative analysis over both short (120–180 s) and full (120–657 s) intervals showed significant differences between day 0 and later time points, with higher exponential wash-out rates on days 3–9 ($p < 0.0001$). Analysis at 800 nm, which provided superior signal-to-noise compared with 780 nm due to an in vivo red-shift of ICG absorption, reproduced these findings. These results indicate that single-wavelength DCE-PAI at 800 nm is sufficient for quantitative perfusion assessment without spectral unmixing.

 doi:10.20944/preprints202603.1150.v1

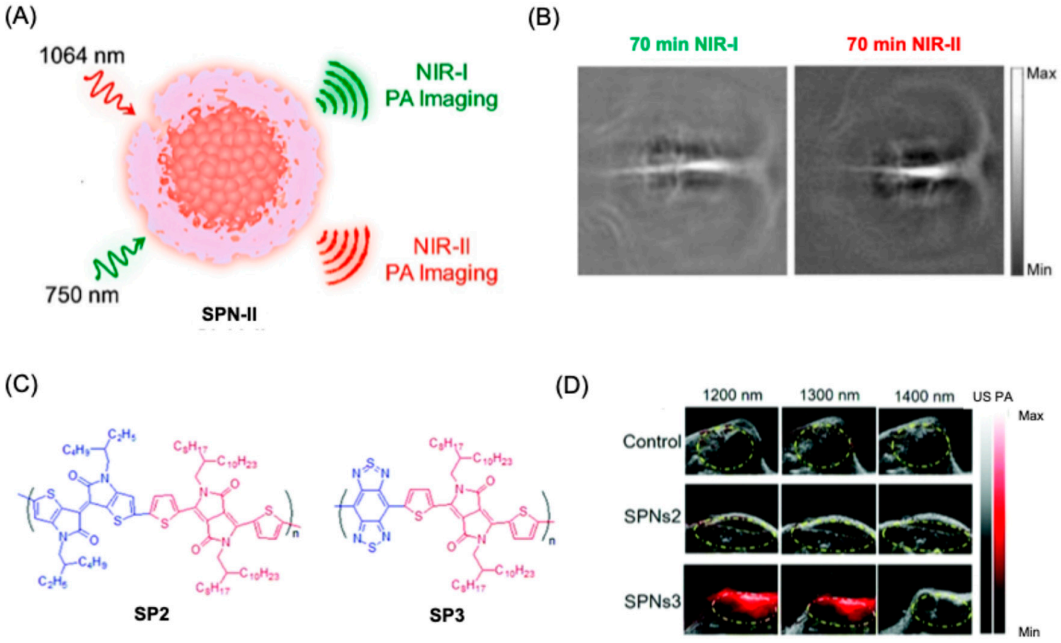

Figure 7. NIR-II organic probes for photoacoustic imaging. (A) Schematic illustration of SPN-II nanoparticles for NIR-II PAI applications. (B) Representative PA images of the rat cortex acquired 70 min after intravenous administration of SPN-II, recorded at 750 and 1064 nm. SPN-II was injected via the tail vein at a dose of 1.8 mg per rat (n = 3). Reproduced with permission from [152]. Copyright 2017, American Chemical Society. (C) Chemical structure of the semiconducting polymer materials used for NIR-II imaging. (D) PA/ultrasound co-registered images of tumors without SPNs2–3 injection (control) and after intratumoral injection of SPNs2–3 (50 μL, 500 μg mL^{-1}). Dashed circles indicate the tumor region. Reproduced with permission from [154]. Copyright information 2019, RSC publishing group. .

In another study, Chen et al. used DCE-PAI for photothermal stimulation of nanoparticles for tumor ablation studies [157]. PNIPAM polymers were loaded with AuNR and CuS spheres. After heating above LCST, the nanogels shrink in size, and at room temperature, they show average diameter of 700 nm (±70 nm). PAI showed PNIPAM AuNR generated PA signal intensity 3.5 times higher than that of AuNR alone. Once the temperature exceeds the LCST, it shows an abrupt additional intensity enhancement of 2.5 times. This increment happens as the temperature transitions from 27 to 32 °C, near the LCST of PNIPAM. Similar photoacoustic signal characterization is performed using PNIPAM-CuS nanoconstructs and CuS NSs alone. The spherical nature of CuS NSs provides PNIPAM-CuS with a better photothermal stability than PNIPAM-AuNR, which can contribute to an improved repeatability as reusable stimuli-responsive agents. Although its trend in photoacoustic intensity increase is similar to that of PNIPAM-AuNR, the enhancement factor of PNIPAM-CuS is slightly different: 2- and 5.5-times clustering enhancements are observed at background temperatures lower and higher than the LCST, respectively. This difference can be attributed to the inherently lower absorption cross-section of the CuS NSs, which requires the nanoparticles to pack more densely to achieve a comparable signal enhancement.

6. Application of PAI for Gynecological Disorders

Gynecological diseases represent a major global health concern, with some conditions leading to severe complications such as infertility [2]. Disorders such as vaginitis affect nearly 75% of women worldwide at least once in their lifetime, while gynecological cancers—including ovarian and cervical cancers—continue to pose significant clinical challenges. For example, ovarian cancer is diagnosed in approximately 314,000 women globally, and despite advances in treatment, the five-year survival

 doi:10.20944/preprints202603.1150.v1

rate remains below 50%[158]. Similarly, cervical cancer accounted for around 604,000 new cases and 342,000 deaths worldwide in 2020, primarily caused by oncogenic strains of human papillomavirus (HPV), particularly types 16 and 18[159]. These statistics highlight the urgent need for improved diagnostic and therapeutic strategies.

Gynecological diseases are broadly categorized into inflammatory conditions and tumors. Inflammatory disorders such as vaginitis, cervicitis, and endometritis are often caused by infections or hormonal imbalances, whereas tumors include cancers of the cervix, ovary, vulva, and endometrium. Current treatments mainly involve antibiotics, antifungal drugs, surgery, chemotherapy, radiotherapy, targeted therapy, and immunotherapy[160]. However, these conventional treatments face several limitations, including drug resistance, poor targeting ability, high recurrence rates, and systemic toxicity[161–163]. In addition, many gynecological tumors remain asymptomatic during early stages, and inadequate screening methods often result in diagnosis at advanced stages[164]. The nonspecific distribution of small-molecule chemotherapeutic agents following intravenous administration further reduces drug accumulation at tumor sites while increasing systemic side effects[165]. These challenges highlight the urgent need for minimally invasive diagnostic tools, targeted therapies, and real-time monitoring strategies to improve treatment outcomes while preserving fertility and minimizing off-target side effects.

In this context, advanced imaging technologies play a crucial role in improving early detection and treatment monitoring. Among these, PAI has emerged as a promising non-invasive technique. PAI enables deep-tissue visualization, high spatial resolution, and molecular-level detection of disease biomarkers, making it particularly valuable for early screening and diagnosis, prognostic assessment, and real-time monitoring of therapeutic responses in gynecological disorders. By integrating targeted molecular probes with PAI, it may become possible to detect inflammatory processes and tumors at earlier stages, ultimately improving clinical outcomes for patients with gynecological diseases.

6.1. PAI for Uterine and Endometrial Microvessel Disorders

Complementing biological and nanomaterial-focused studies, system-level developments have addressed the practical requirements for noninvasive pelvic imaging. Photoacoustic spectroscopy and hybrid ultrasound–photoacoustic platforms designed for abdominal cavity imaging emphasize the importance of illumination geometry, acoustic detection sensitivity, and real-time imaging capability for clinical deployment [27]. Related work in adjacent uterine pathologies, such as intrauterine adhesions, further supports the value of functional photoacoustic metrics, including oxygenation and perfusion, for grading disease severity, suggesting that similar quantitative biomarkers could be adapted for endometriosis assessment [166]. Intrauterine adhesion (IUA) is the secondary reason for infertility in women. In a recent study, Dong et al. showed that endometrial oxygen saturation can correlate with IUA using PAI, overcoming limitations of ultrasound-only diagnosis (**Figure 8A**)[166]. In this study, IUA was established in a rat model through mechanically induced uterine injury to mimic fibrosis and adhesion formation. The animals were subsequently examined using both PAI and high-frequency ultrasound imaging to compare diagnostic performance. Ultrasound imaging provided anatomical visualization of the uterine structure, while PAI measured hemoglobin-related optical absorption signals to assess vascularity and tissue oxygenation. The results showed that adhesion regions exhibited reduced vascular signals and altered oxygenation patterns, which PAI detected more clearly than by ultrasound alone. Quantitative analysis demonstrated that PAI enabled more sensitive evaluation of adhesion severity and functional tissue changes, highlighting its advantage for noninvasive assessment and monitoring of IUA (**Figure 8B**).

Endometrial microvessels provide oxygen and nutrients to the embryo, and they are of significant importance in evaluating endometrial receptivity. Endoscopic PAI is used to study such microvessel systems, which enabled real-time, high-resolution visualization of endometrial microvessels and blood perfusion using endogenous hemoglobin contrast, outperforming

 doi:10.20944/preprints202603.1150.v1

conventional ultrasound in functional vascular assessment [167]. **Figure 8C-I** compares endometrial microvascular imaging in normal rats using multiple imaging modalities. The endometrium exhibited a dense, basket-like vascular organization consistent with previously reported anatomical observations. MicroCT imaging following contrast administration provided a macroscopic overview of uterine vasculature; however, fine microvascular structures were not clearly resolved in either the original or magnified views (**Figure 8C**). In contrast, PAI enabled detailed visualization of the endometrial vascular network, with three-dimensional reconstructions revealing continuous microvessel architecture (**Figure 8D**). Compared with the 3D datasets, two-dimensional photoacoustic slices displayed partial vessel discontinuity due to limited sectional information (**Figure 8E**). Histological validation using CD31 staining confirmed the abundance of superficial endometrial microvessels, although detailed structural morphology could not be fully appreciated from histology alone (**Figure 8F**). Sequential B-scan imaging using endoscopic ultrasound, PAI, and their merged outputs further demonstrated depth-resolved vascular patterns, clearly revealing microvessel distribution within the tissue (**Figure 8G-I**). Signal analysis indicated that the strongest photoacoustic response originated from a depth of approximately 1.22 mm, corresponding to an effective imaging penetration of at least 470 μm.

6.2. PAI for Endometriosis

Endometriosis (EM) is a common gynecological condition in which endometrial-like tissue grows outside the uterus, leading to chronic pelvic pain, infertility, and reduced quality of life for millions of women globally[10,102,168]. Despite its prevalence and clinical burden, EM remains difficult to diagnose, often resulting in prolonged diagnostic delays and disease progression. Conventional imaging tools, including ultrasound, MRI, and CT, have been used for decades but exhibit notable limitations. CT is primarily useful for thoracic manifestations but is less sensitive for pelvic lesions. MRI can identify deep-infiltrating disease but requires cycle-dependent timing, pharmacological bowel suppression, and still fails to reliably detect small or superficial lesions. Ultrasound is similarly constrained

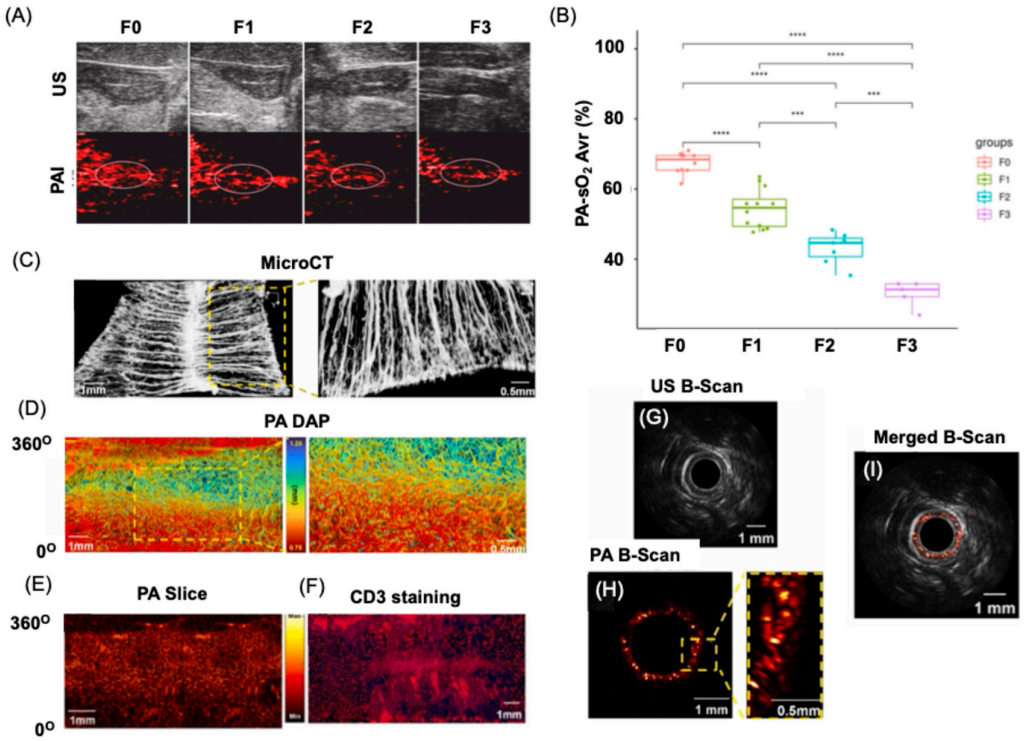

 doi:10.20944/preprints202603.1150.v1

Figure 8. Application of PAI for uterine diseases. (A) Representative images from ultrasound and PAI in control rats (F0) and rats with mild (F1), moderate (F2), and severe endometrial fibrosis (F3). The dotted circle shows the area where the fibrosis. (B) Represents the box plot indicating the PA oxygen saturation in each case. ∗P < .05, ∗∗P < .01, ∗∗∗P < .001. Reproduced with permission from [166]. Copyright 2024, Elsevier. (C-I) Microvessels in normal rat endometrium visualized using multiple imaging modalities. (C) MicroCT image with corresponding magnified region. (D) Photoacoustic DAP image with magnified view. (E) Photoacoustic slice at ~300 μm depth. (F) CD31 immunostaining of microvasculature. (G–I) Ultrasonic (US) B-scan, photoacoustic (PA) B-scan with magnified region, and merged US/PA B-scan image. Yellow boxes indicate representative microvessel regions. US: ultrasound; PA: photoacoustic imaging. Reproduced with permission from [167]. Copyright 2024, Elsevier. .

by poor contrast between lesions and surrounding tissues. As a result, laparoscopic surgery with histological confirmation remains the diagnostic gold standard, despite its invasiveness and associated risks[4,169]. These challenges underscore the urgent need for sensitive, specific, and non-invasive imaging strategies for early EM detection.

Recent progress in biomedical imaging has introduced new opportunities to improve EM diagnosis and better understand disease pathology[169]. Targeted nanoparticle-based approaches, such as magnetic nanoparticles functionalized with RGD peptides or folate ligands, have shown promise for lesion localization using MRI[170]. Among emerging modalities, PAI has attracted particular interest due to its ability to combine optical contrast with ultrasonic resolution, enabling real-time, deep-tissue imaging. This technique can leverage endogenous absorbers, such as hemoglobin and lipids, to visualize vascular and compositional features of tissue. EM lesions, which undergo cyclic bleeding, exhibit distinct optical absorption signatures that have been successfully visualized using PAI in preclinical models. However, reliance on endogenous contrast, particularly at visible wavelengths such as 532 nm, limits penetration depth and reduces sensitivity for deeply located or weakly vascularized lesions. Additionally, some EM lesions lack sufficient intrinsic optical contrast, making them difficult to distinguish from surrounding tissue. To address these limitations, exogenous contrast agents have been explored to enhance photoacoustic signal strength, spectral tunability, and target specificity. Nanoparticle-based contrast agents enable high signal-to-noise lesion visualization and can be engineered to target molecular markers associated with EM pathogenesis [12,20,75]. Beyond imaging, such nanoparticles can also serve therapeutic functions. Gold -based nanomaterials efficiently convert near-infrared light into localized heat, enabling photothermal ablation of diseased tissue while sparing adjacent healthy structures [16]. This dual diagnostic–therapeutic capability highlights the potential of nanoparticle-enabled PAI as a powerful platform for non-invasive detection and treatment of endometriosis.

6.2.1. PAI for Noninvasive Detection of Endometriosis

Recent preclinical studies demonstrate that both endogenous and exogenous photoacoustic contrast mechanisms can be exploited to detect, characterize, and monitor endometriotic lesions[15,171]. Early work using photoacoustic microscopy established the feasibility of imaging endometriosis-associated vascular remodeling in murine models by leveraging endogenous hemoglobin contrast [172]. These studies revealed distinct microvascular patterns and perfusion characteristics associated with lesion development, highlighting the potential of label-free PAI to probe lesion biology. As shown in **Figure 9A-B**, after subcutaneous implantation of endometriosis, a nodule was observed in the skin 10 days later. The PAM studies revealed the maximum amplitude projection (MAP) images of the region of interest (ROI), outlined in yellow dotted lines, indicated that the lesion was surrounded by prominent blood vessels, as indicated by yellow arrows in **Figure 9B**. Corresponding B-scan images (**Figure 9D-E**), obtained along the dashed lines D and E shown in **Figure 9C**, demonstrated strong PA signals originating from the lesion (red arrows) at depths exceeding 1 mm beneath the epidermal surface. Notably, the PA signal intensity from the lesion was significantly higher than that of the surrounding tissues, except for vascular signals. Subsequent

 doi:10.20944/preprints202603.1150.v1

hematoxylin and eosin (H&E) staining together with immunohistochemical analyses (**Figure 9F–I**) confirmed the presence of endometriotic glandular and stromal morphogenesis within the targeted lesion. In addition to the MAP imaging results, three-dimensional reconstruction and visualization of the lesion were also performed. However, microscopy-based implementations are inherently limited in penetration depth, restricting their applicability to superficial or surgically exposed tissues and motivating the development of deeper-tissue PAI strategies more relevant to pelvic disease.

To overcome sensitivity and depth limitations, contrast-enhanced PAI approaches employing nanoparticles have been introduced [173,174]. Gold nanorod (AuNR)–based labeling approaches have enabled robust visualization of lesions when combined with ultrasound co-registration, facilitating longitudinal imaging and multimodal validation through complementary fluorescence signals. Ryan et al. prepared AuNRs labelled with FITC(fluorescein isothiocyanate) as multimodal imaging agents for endometriosis [173]. They have prepared a stitch model for making the endometriosis, where the uterine horn tissue fragments were supplemented with AuNR-FITC NPs (**Figure 9J**). The nanoparticle-labeled tissue was injected into the peritoneal cavity of the recipient mice for the endometriosis development (**Figure 9J**). After four weeks of lesion establishment, noninvasive whole-body PAI imaging was performed, followed by fluorescence-guided lesion isolation. In mice bearing AuNR-FITC nanoparticle–labeled lesions, strong gold-associated PA signals were detected and colocalized with oxyhemoglobin and deoxyhemoglobin signals, whereas no comparable signals were observed in control animals (**Figure 9K**). These results indicate selective nanoparticle accumulation within highly vascularized endometriosis-like lesions. Quantitative analysis confirmed a significant increase in gold-derived

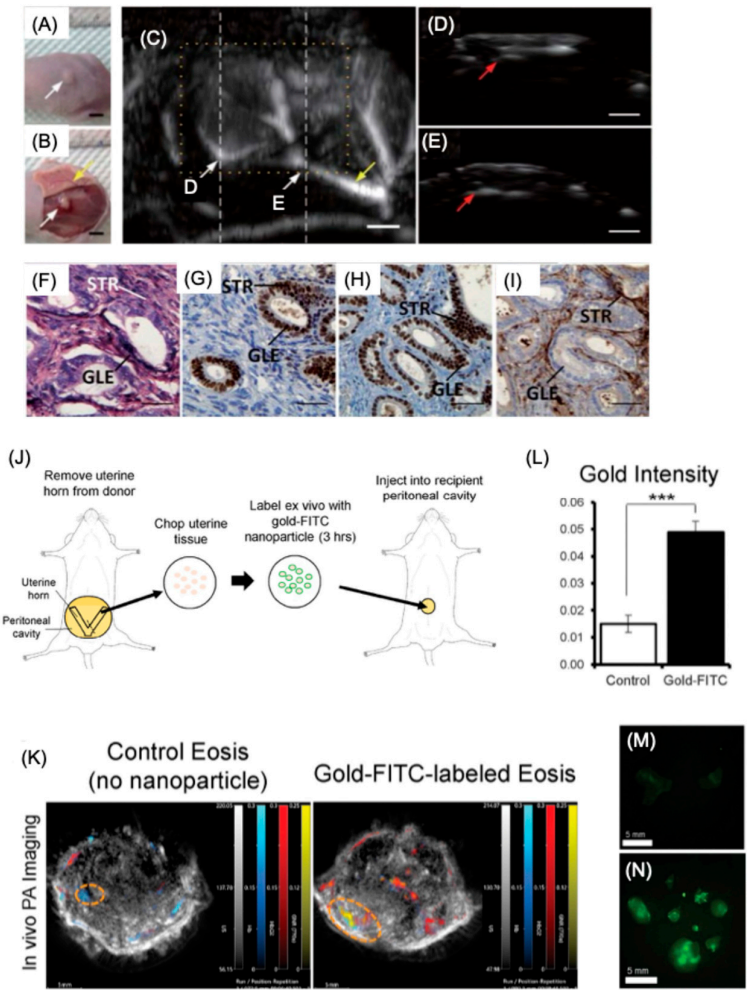

 doi:10.20944/preprints202603.1150.v1

Figure 9. PAI application for endometriosis. (A) Positive identification of the endometriosis lesion using PA microscopy. (A–B) Macroscopic images of the EM lesion (white arrows) before and after anatomical dissection. (C) MAP image showing the EM lesion and surrounding blood vessels. (D–E) Corresponding B-scan images from the regions marked in (B) (F) H&E staining. (G–I) Immunohistochemical staining for PR, ER, and CD10. GLE: glandular epithelial cells; STR: stromal cells. Scale bars: (A–B) 5 mm; (C–E) 1 mm; (F–I) 50 μm. Reproduced with permission from [172]. Copyright 2014, Wiley Publishers. (J) Schematic of the surgical induction of endometriosis in mice using gold–FITC nanoparticle–labeled uterine tissue. (K) Representative in vivo PA images from control mice (no nanoparticles, left) and mice with gold–FITC nanoparticle–labeled lesions (right), showing PA signals for gold (yellow), Hb (blue), and HbO_2 (red) four weeks after induction. Orange dashed circles indicate lesions identified by dissection (left) or detected by PA imaging and confirmed by dissection (right). Scale bar = 5 mm. (L) Quantification of gold PA signal intensities from ROIs around endometriosis lesions (mean ± SEM; control n = 4, gold–FITC NP n = 3; ***$p < 0.001$). PA signals were co-registered with B-mode ultrasound images (gray). (M-N) FITC fluorescence images of control and gold–FITC nanoparticle–labeled lesions after lesion dissection four weeks post-induction. Green fluorescence indicates nanoparticle presence. Scale bar = 5 mm. Reproduced with permission from [173]. Copyright 2022, Springer Publishers. .

signals in labeled tissues compared with controls ($p = 0.0004$; **Figure 9L**), while local oxygen saturation remained unchanged ($p = 0.9538$). Post-dissection imaging verified FITC-positive lesions in the peritoneal cavity only in nanoparticle-labeled mice (**Figure 9M-N**). In addition, the combined PA–ultrasound platform enabled the detection of implanted embryos as early as gestation day 7.5 based on anatomical ultrasound contrast and hemoglobin-derived PA signals, allowing longitudinal monitoring of pregnancy alongside lesion imaging. Together, these studies demonstrate that nanoparticle-enhanced PAI can markedly improve lesion conspicuity beyond endogenous contrast alone, particularly for deeper or smaller lesions.

6.2.2. Endometriosis Treatment Validation Using PAI

Beyond detection, PAI has also been explored as a theranostic platform for endometriosis. Polydopamine-based nanoparticles modified with targeting ligands, such as hyaluronic acid (PDA@HA), have been shown to significantly enhance photoacoustic signal intensity within endometriotic lesions in vivo[174]. This strategy capitalizes on the strong broadband NIR absorption and photothermal efficiency of polydopamine while leveraging biological interactions within lesion microenvironments to improve localization. In vivo PAI was conducted in C57BL/6J mice with intraperitoneal lesions. Following intravenous injection of PDA@HA nanoparticles, photoacoustic signals were recorded at 2, 4, 8, 12, and 24 h (**Figure 10A**). Signal enhancement was mainly observed along the upper boundaries of the lesions (**Figure 10B**), while anatomical reference images were simultaneously obtained using ultrasound (US) (**Figure 10C-D**). Background signals detected at the skin surface were attributed to endogenous chromophores such as melanin. Quantitative analysis (**Figure 10B**) showed a gradual increase in PA intensity, reaching a maximum at 8 h post-injection, followed by a decline to approximately 32% of peak intensity at 24 h. These results indicate time-dependent nanoparticle accumulation and subsequent clearance, identifying 8 h as the optimal imaging time point. Combined US–PAI imaging further improved lesion delineation. Cystic lesions exhibited low ultrasonic echogenicity but were clearly defined in merged images (**Figure 10C-D**), with strong spatial agreement between modalities. Moreover, PAI enhanced visualization of lesions with weak US contrast, particularly at their superficial margins (**Figure 10D**). Together, these findings demonstrate that PDA@HA-assisted PAI effectively images orthotopic lesions with diverse ultrasonic characteristics. Owing to the high photothermal conversion efficiency ≈28%, these NPs were studied for the treatment of endometriosis by measuring lesion size using a US-PAI system (**Figure 10E**).

Silica-coated gold nanorods (AuNRs) have been explored as both photoacoustic contrast agents and photothermal transducers for targeted ablation of endometriosis lesions. Kumar et al. developed FITC-labeled silica-coated gold nanorods (AuNR@Si(F)-PEG) with a fluorescence quantum yield of

 doi:10.20944/preprints202603.1150.v1

0.13, enabling in vivo fluorescence detection of lesions (**Figure 10F**)[16]. The strong NIR absorption of AuNR enhanced PAI, while the silica shell improved nanoparticle stability and photothermal conversion efficiency (~52.1%). Following intravenous administration, strong fluorescence signals from FITC were observed at lesion sites and confirmed by lesion excision and tissue staining (**Figure 10G–H**). After four weeks of lesion development, noninvasive whole-body PAI followed by fluorescence-guided excision was performed. As shown in **Figure 10I**, strong AuNRs' photoacoustic signals colocalized with total hemoglobin (HbT), indicating nanoparticle accumulation in highly vascularized ectopic tissues. Signal intensity peaked at ~2 h post-injection and gradually decreased, with clearance by 48 h. Quantitative analysis confirmed significantly higher signals at 2 h compared with pre-injection and later time points. Ex vivo biodistribution analysis using fluorescence imaging and ICP-OES revealed the highest Au accumulation in the liver (28.2 μg g^{-1}), followed by endometriosis lesions (12.8 μg g^{-1}), while spleen and kidney showed lower uptake (~2.4 μg g^{-1}). Minimal Au was detected in lungs, heart, and uterus. Owing to the strong photothermal properties of AuNR, lesions were ablated using an 808 nm laser, resulting in a ~77% reduction in lesion volume as measured by US-PAI and by histological studies. Overall, PAI enables real-time visualization of lesion distribution before therapy and monitoring of treatment response through vascular changes after ablation. This image-guided "diagnose-and-treat" strategy is promising for endometriosis, where localized therapy and preservation of surrounding reproductive tissues are essential. However, challenges such as thermal dose control, off-target heating, and long-term safety remain. In another study, Rahman et al. showed the use of ICG-conjugated nanoceria for theranostics of endometriosis using PAI [102]. Owing to the anti-inflammation property of nanoceria, a reduced number of lesions were observed in the nanoparticle-treated group compared to the control groups. Moreover, there were no adverse effects for the pregnancy in mice using this nanoparticle as compared with tofacitinib, which showed potential infertility for long-term use.

Collectively, existing studies position PAI as a promising modality for endometriosis research and diagnosis. Endogenous PAI provides valuable insight into lesion vascular physiology, while nanoparticle-enhanced and theranostic approaches expand sensitivity and functional scope. Future progress will depend on improving molecular specificity, standardizing quantitative imaging metrics, and integrating PAI with clinically established ultrasound workflows. With continued advances in contrast agent design, biomarker selection, imaging hardware, and validation in clinically relevant models, PAI has strong potential to evolve into a noninvasive tool for detection, therapy guidance, and longitudinal monitoring of endometriosis.

6.3. Cervical Tissue Remodeling and Pregnancy-Related Conditions

The human cervix is a dynamic tissue composed of smooth muscle, epithelial cells, fibroblasts, and blood vessels embedded within a collagen-rich extracellular matrix primarily consisting of type I and type III collagen, elastin, and proteoglycans [175]. During pregnancy, progressive cervical remodeling alters tissue stiffness and length through reorganization of the collagen network, increased hydration, extracellular matrix degradation, and enhanced vascularity. These structural and biochemical changes intensify as delivery approaches, and premature cervical shortening is strongly associated with an increased risk of preterm birth [176]. Evidence suggests that early disruption or disorganization of cervical collagen architecture contributes to abnormal remodeling and may serve as an important predictor of preterm delivery [177]. PAI enables functional assessment of cervical remodeling by quantifying changes in vascularity and oxygenation associated with collagen reorganization, providing complementary information beyond conventional ultrasound-based cervical length measurements.

 doi:10.20944/preprints202603.1150.v1

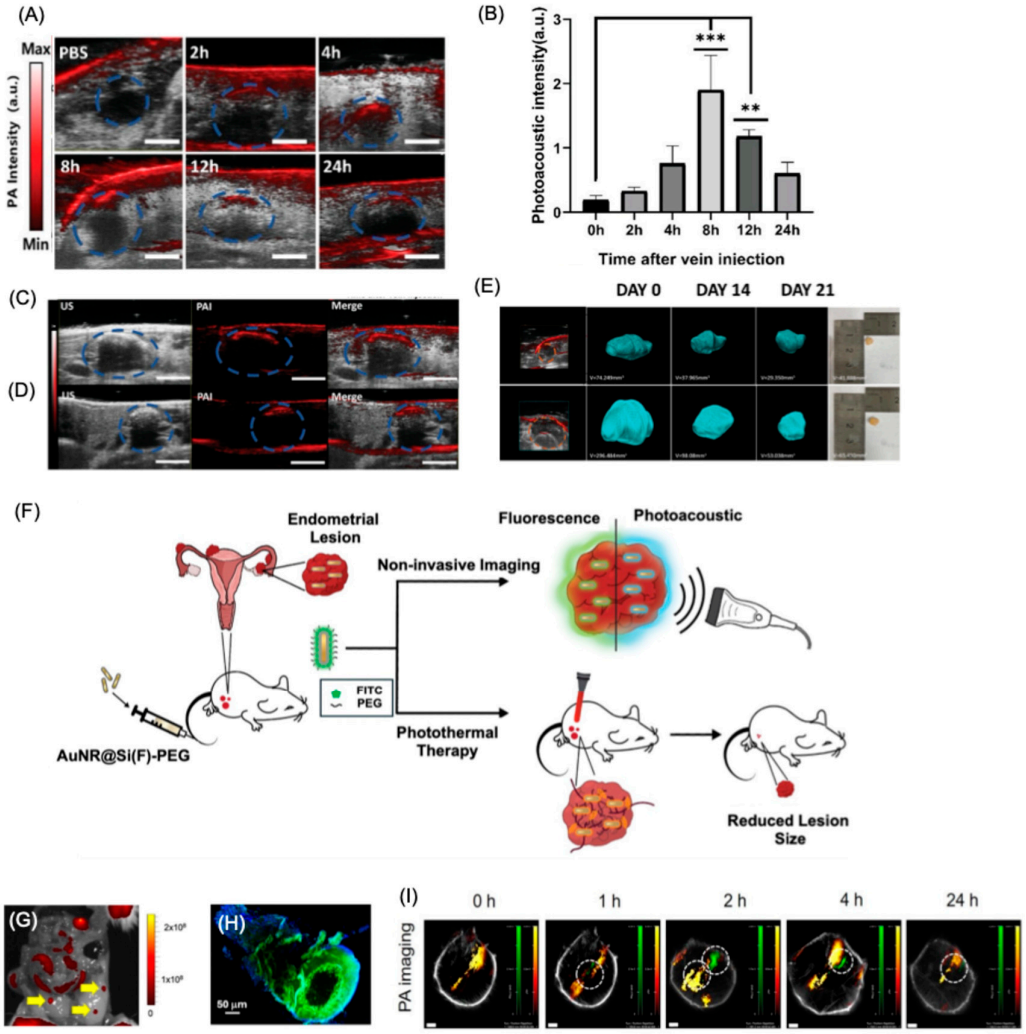

Figure 10. Application of PAI for endometriosis diagnosis and treatment. (A) PAI of endometriosis lesions after injection of PBS or PDA@HA at 2, 4, 8, 12, and 24 h. (B) Quantification of time-dependent PA signal intensity in lesions (p-value: 8 h: ***p < 0.001,12 h: **p = 0.006; n = 3 per group). (C) Representative US, PAI, and merged images of lesions showing distinct acoustic scattering variation. (D) US, PAI, and merged images of lesions without noticeable acoustic scattering variation (scale bar: 4 mm). (E) Lesion volumes measured by US–PAI at days 0, 14, and 21 after PBS or treatment, with corresponding photographs of excised lesions (orange dashed circles indicate lesions; n = 4 per group). Reproduced with permission from [174]. Copyright 2024, Wiley Publishers. (F) Schematic for the working principle for AuNR@Si(F)-PEG NPs for endometriosis detection and treatment. (G) IVIS Spectrum in vivo imaging of a systemic mouse model used to validate endometriosis-like lesions following intravenous injection of AuNR@Si(F)-PEG nanoparticles. (H) Fluorescence microscopy images confirming endometriosis lesions after excision from mice. Blue = DAPI; green = FITC. (I) Representative in vivo PA images from the endometriosis lesions in mice with AuNR@Si(F)-PEG NPs at different time intervals. AuNR (green), HbT (orange red). Reproduced with permission from [16]. Copyright 2025, Wiley Publishers.

Yan et al. studied the collagen-to-water ratio (CWR) in cervical tissue compositions excised human samples tissues using PAI [175]. The study compared cervical tissues from pregnant (21–36 years, median 30) and non-pregnant hysterectomy patients (29–58 years, median 42) to evaluate structural and compositional differences using spectroscopic photoacoustic (sPA) imaging and histology. Averaged sPA spectra revealed that non-pregnant cervical tissues exhibited strong collagen-associated photoacoustic peaks within the 1150–1250 nm range, whereas pregnant tissues showed higher signal amplitudes in the water-dominant region (1300–1650 nm), indicating increased

 doi:10.20944/preprints202603.1150.v1

tissue hydration. Histological analyses (H&E and Sirius Red staining) confirmed these findings, demonstrating dense, well-organized collagen bundles in non-pregnant samples compared to loose collagen architecture with edema in pregnant tissues. Quantitative wavelength unmixing showed significantly higher collagen-to-water ratio (CWR) in non-pregnant women (55.0% ± 20.3%) than in pregnant women (18.7% ± 7.5%; $p = 0.00016$). Subgroup analysis of patients under 41 years further validated this difference, supporting pregnancy-associated collagen remodeling and increased water content in cervical tissue. The developed imaging platform has the potential to enable accurate and reliable screening and diagnostic assessment with improved sensitivity and specificity, facilitating early detection of cervical insufficiency and offering a promising approach for predicting the risk of preterm birth.

A dual-illumination US/PAI system was developed by Basiji et al. to enhance cervical cancer detection. The study demonstrated that cancerous cervical tissues produced higher photoacoustic signal amplitudes compared to normal tissues, due to increased hemoglobin content and tumor-associated vascularization [178]. Dual-sided light delivery improved optical penetration and signal uniformity, enabling more reliable visualization of deep cervical regions. The integrated imaging approach allowed simultaneous anatomical localization and functional assessment of tissue composition. These findings highlight the potential of PAI as a noninvasive modality for early diagnosis and characterization of cervical cancer. The same group studied the biochemical and structural changes in the uterine cervix during murine pregnancy by quantifying collagen and water content [179]. Spectroscopic photoacoustic (sPA) measurements revealed a progressive decrease in collagen-associated signals, accompanied by increased water-related signals, reflecting pregnancy-induced cervical remodeling. These findings were validated by histological staining, which showed collagen disorganization and increased tissue hydration during gestation. The study demonstrated that PAI enables noninvasive, label-free monitoring of cervical softening processes. This approach highlights the potential of PAI for assessing cervical maturation and predicting pregnancy-related complications such as preterm birth.

Spectral PAI was utilized to evaluate age-related collagen remodeling in the reproductive tract using a mouse model of pelvic organ prolapse [180]. In a study by Markel et al. a wavelength-dependent PAI analysis revealed a significant reduction in collagen-associated photoacoustic signals in aged mice compared with young controls, indicating loss of collagen density and structural integrity. Their quantitative spectral unmixing demonstrated decreased collagen-to-water ratios (CWR) and altered tissue composition consistent with age-associated extracellular matrix degeneration. These photoacoustic findings were corroborated by histological analyses showing disrupted collagen organization and reduced fiber alignment in prolapsed tissues. Collectively, the results demonstrate that spectral PAI enables noninvasive, label-free assessment of collagen degradation and provides a promising tool for monitoring tissue remodeling associated with aging and pelvic organ prolapse.

6.4. Ovarian Pathologies

Diagnosis of ovarian cancer and lesions is challenging due to the heterogeneity in clinical reports [181]. Non-invasive detection techniques, such as US/PAI, can be used for the early detection of such disease conditions [182–184]. In one of the studies, optical-resolution photoacoustic microscopy (OR-PAM) combined with a vascular graph network was developed for automated classification of ovarian lesions based on microvascular architecture[182]. The study extracted quantitative vascular features, including vessel density, branching patterns, and network topology, from high-resolution photoacoustic images to characterize lesion-associated angiogenesis. As shown in **Figure 11A**, the vasculature in normal ovaries was very thin and sparsely distributed. But the ovarian lesions showed abnormalities and morphological deformations under different pathological conditions. The graph-based deep learning model achieved accurate differentiation between normal and pathological ovarian tissues by leveraging vascular structural information derived from photoacoustic signals. As shown in **Figure 11B**, the classification performance of the vascular graph network (VGN) at the

 doi:10.20944/preprints202603.1150.v1

individual graph level demonstrates strong diagnostic accuracy across different ovarian tissue types. The model achieved the highest sensitivity and specificity in distinguishing normal ovaries and benign solid lesions. Importantly, the system showed robust capability in differentiating malignant tumors from benign pathologies, which is critical for clinical diagnosis. Analysis of vascular grafts derived from cancerous tissues yielded a sensitivity of 0.795 ± 0.022 and an area under the curve (AUC) of 0.877 (95% CI: 0.859–0.891), indicating reliable cancer classification performance. These results highlight the effectiveness of vascular-feature–based photoacoustic analysis for accurate ovarian lesion discrimination. This work highlights the potential of photoacoustic microscopy integrated with artificial intelligence for noninvasive, label-free ovarian cancer diagnosis and automated lesion classification. In another study, the same research group demonstrated the use of OR-PAM for label-free visualization and measurement of vascular parameters, including vessel density, diameter, branching patterns, and spatial organization [183]. The study demonstrated significant vascular heterogeneity in ovarian lesions compared with normal tissues, reflecting disease-associated angiogenic remodeling (**Figure 11C**). Quantitative analysis revealed distinct vascular characteristics that allowed differentiation between pathological and healthy reproductive tissues.

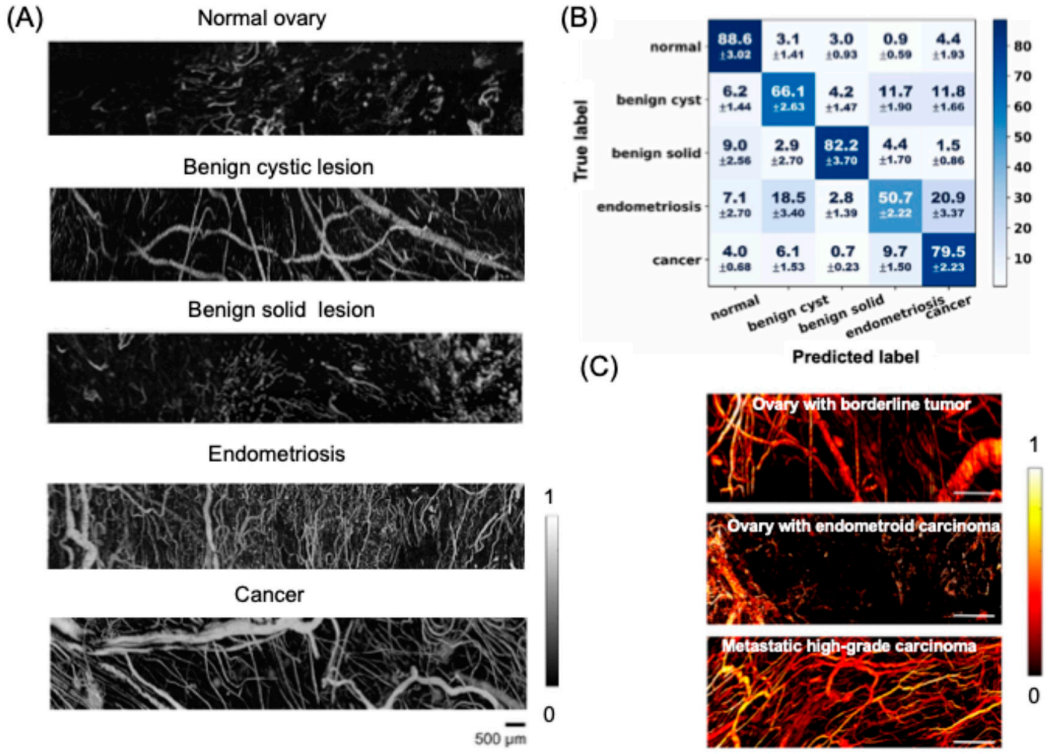

Figure 11. PAI application in ovarian pathologies. (A) OR-PAM images of ovarian lesions representing different pathological conditions, displayed with a 40 dB dynamic range. (B) Performance of VGN for five-class classification. The confusion matrix represents the average of 100 random train–test splits and is normalized by the number of vascular graphs in each category to report sensitivity (%) for each class. Standard deviations derived from cross-validation are shown below the sensitivities to indicate prediction stability**.** Reproduced with permission from [182]. Copyright 2026, Elsevier. (C) Representative micrographs of ovarian and fallopian tube lesions exhibiting different levels of malignancy. Scale bar: 500 μm. Reproduced with permission from [183]. Copyright 2022, Nature Publishing group.

A combined ultrasound–photoacoustic (US/PA) imaging protocol was developed for transvaginal imaging of ovarian lesions to enable simultaneous anatomical and functional assessment.[184]. The integrated approach combined ultrasound-based structural visualization with

 doi:10.20944/preprints202603.1150.v1

photoacoustic detection of hemoglobin-related optical contrast, allowing improved characterization of lesion vascularity. The study demonstrated enhanced visualization of ovarian lesion boundaries and vascular features compared with ultrasound imaging alone. Photoacoustic signals provided additional functional information related to blood content and tissue heterogeneity, facilitating differentiation between lesion types. These results highlight the potential of combined US/PA transvaginal imaging as a noninvasive strategy for improved evaluation and diagnosis of ovarian abnormalities.

7. Clinical Translation and Integration

PAI is steadily advancing toward clinical implementation, driven by the development of probe-based and intraoperative imaging systems designed for real-time use in surgical and diagnostic procedures [29]. The integration of photoacoustic technology with conventional ultrasound platforms has been particularly impactful, enabling simultaneous acquisition of anatomical, functional, and molecular information, while maintaining the familiarity and efficiency of established clinical workflows. Multimodal combinations with optical, Doppler, and spectroscopic imaging further enhance diagnostic capability by providing complementary tissue contrast and quantitative physiological parameters. Importantly, advances in laser safety standards, portable light-delivery technologies, and regulatory-aligned device engineering have improved the feasibility of clinical adoption by addressing safety, usability, and workflow requirements. Together with the emergence of workflow-compatible handheld and transvaginal probes, these advances position PAI as a promising translational modality for intraoperative guidance, disease diagnosis, and real-time clinical decision-making.

PAI community is currently advancing toward greater standardization, a critical step for ensuring reliable clinical translation and multicenter implementation. The International Photoacoustic Standardization Consortium (IPASC) has established consensus guidelines for technical specifications, data-acquisition parameters, and reporting standards to reduce variability between imaging systems[185]. To address inconsistencies in proprietary data formats, standardized metadata structures and an open-source application programming interface were introduced, enabling conversion into a unified format and facilitating data exchange and cross-site comparison. These initiatives have also accelerated the integration of PAI data into the Digital Imaging and Communications in Medicine (DICOM) framework, thereby improving compatibility with existing clinical imaging infrastructure[73,74,186]. Ongoing efforts include the development of open-source image-reconstruction libraries that enable systematic evaluation of algorithm performance, particularly as artificial intelligence methods become increasingly integrated into PAI data analysis. In parallel, consensus terminology, imaging-biomarker definitions, and image-quality metrics are being established to harmonize communication across research and clinical communities. Furthermore, recognizing the need for reproducible validation, standardized tissue-mimicking phantoms and testing protocols are being developed to provide reliable ground-truth datasets for performance assessment, quality assurance, and system calibration. Although full clinical standardization is still underway, the technical similarity of PAI to ultrasound and its favorable safety profile have already enabled early clinical studies and multicenter investigations. Continued progress will require coordinated regulatory alignment, standardized clinical training programs, and close collaboration among engineers, researchers, and healthcare professionals to ensure safe and consistent clinical adoption.

Several PAI platforms have been translated toward clinical use. Representative systems include multispectral optoacoustic tomography (MSOT) devices such as the Acuity Echo platform, hybrid ultrasound–photoacoustic systems such as the Imagio breast imaging system, and emerging mesoscopic systems including raster-scan optoacoustic mesoscopy (RSOM). In addition, handheld probes and endoscopic photoacoustic devices are under development to enable real-time clinical imaging and image-guided interventions. **Table 3** represents the major clinical approved PAI systems and their applications.

 doi:10.20944/preprints202603.1150.v1

Table 3. Clinical Status of Major PAI Systems.

System	Clinical Status	Notes
MSOT Acuity / Acuity Echo (iThera Medical)	Clinical research / human trials	Used in clinical research centers for imaging inflammation, cancer, and vascular disease.
Imagio Breast Imaging System (Seno Medical)	FDA-cleared clinical device	Used clinically for breast lesion evaluation alongside ultrasound.
RSOM Explorer	Clinical research device	Used in human studies for dermatology and microvascular imaging.
Twente Photoacoustic Mammoscope	Clinical research prototype	Used in clinical breast cancer imaging trials.
Photoacoustic Endoscopy systems	Preclinical / early translational research	Still mainly experimental but progressing toward human trials.
Handheld PAI probes	Clinical research prototypes	Used in several pilot clinical studies but not yet standard devices.

PAI has shown strong performance in preclinical small-animal studies and is increasingly transitioning toward clinical applications. Several commercial PAI platforms have also emerged to support this transition[187]. Although implementations vary, three primary configurations dominate current clinical investigation according to the anatomical region of interest and diagnostic objective: dual-modal photoacoustic–ultrasound imaging (PAUSI), station-based tomographic PAI, and mesoscopic/microscopic PAI [29,72].

Dual-modal PAUSI integrates a conventional ultrasound imaging (USI) system with a portable pulsed laser, allowing simultaneous acquisition of ultrasound and photoacoustic signals (**Figure 12A**). This approach provides complementary information on tissue structure and blood flow from ultrasound, while adding optical absorption–based contrast from photoacoustics, such as hemoglobin concentration, oxygen saturation, and molecular probe distribution. PAUSI systems can be configured as handheld or endoscopic devices. Handheld systems typically employ linear, phased, or curvilinear ultrasound arrays coupled with optical fiber bundles and are commonly used for imaging superficial tissues, including the skin, thyroid, breast, and limbs. Endoscopic PAUSI systems, incorporating transrectal or transvaginal probes with miniaturized optical fibers, enable imaging of internal organs and facilitate the diagnosis of rectal and gynecological diseases.

Station-based tomographic PAI employs large detection apertures, such as hemispherical or ring-shaped ultrasound transducer arrays, to efficiently capture omnidirectional photoacoustic waves and improve image reconstruction quality (**Figure 12B**). In typical clinical configurations, the detector array is placed beneath the imaging platform and integrated with a pulsed-laser and synchronized ultrasound-acquisition electronics. A motorized stage allows scanning over larger ROIs, expanding clinical applicability. These systems provide relatively deep tissue imaging in humans (up to ~5 cm) while maintaining high spatial resolution, and have been applied to organs such as the brain, breast, and peripheral limbs.

Mesoscopic and microscopic PAI utilize high-frequency single-element ultrasound transducers combined with dark-field or weakly focused optical illumination (**Figure 12C**). The use of high acoustic numerical aperture enables spatial resolution on the order of tens of micrometers, allowing detailed visualization of microvascular and structural features. These systems are typically mounted on articulated arms and acquire three-dimensional images through point-by-point raster scanning using a motorized stage. Owing to their high spatial resolution, mesoscopic and microscopic PAI are

 doi:10.20944/preprints202603.1150.v1

particularly suited for imaging superficial tissues and diagnosing skin disorders such as skin cancer and psoriasis.

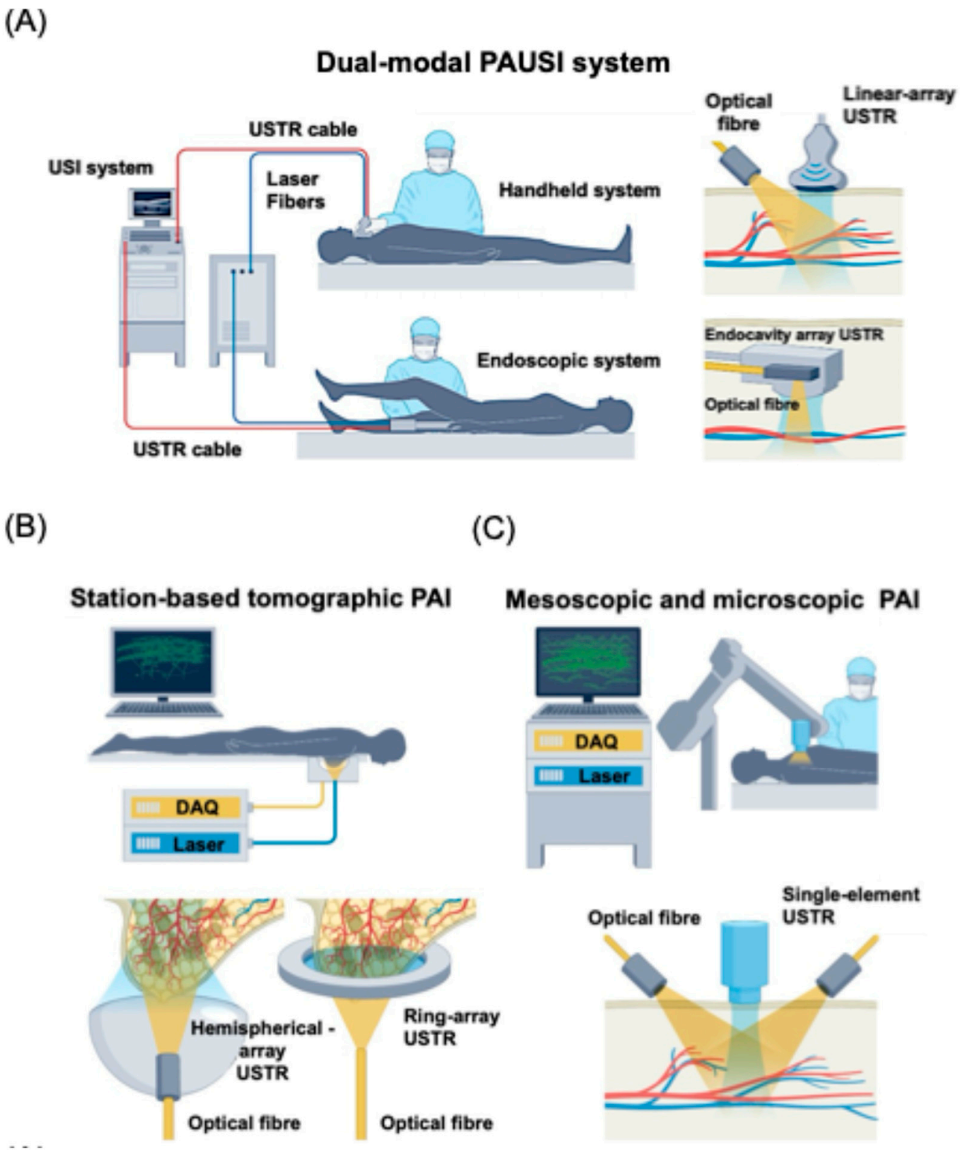

Figure 12. Application of various PAI systems for clinical trials. (A) Dual-modal photoacoustic–ultrasound imaging (PAUSI) systems are derived from conventional ultrasound imaging (USI) platforms and are generally implemented in two formats: a handheld configuration employing linear-array ultrasound transducers (USTRs) and an endoscopic configuration utilizing endocavity array transducers. Handheld systems are primarily used for imaging superficial tissues such as the skin, thyroid, breast, and peripheral limbs. In contrast, endoscopic implementations enable imaging of internal regions, including the stomach, vaginal canal, and rectum. (B) Station-based tomographic PAI employs hemispherical or ring-shaped ultrasound transducer arrays, which allow efficient detection of photoacoustic signals for tomographic reconstruction. These systems are mainly applied to imaging brain, breast, and limb tissues. (C) Mesoscopic and microscopic PAI utilize high-frequency single-element ultrasound transducers, enabling high-resolution imaging. This configuration is particularly suited for examining superficial tissues such as skin. Reproduced with permission from [29]. Copyright 2024, Nature Publishing Group.

 doi:10.20944/preprints202603.1150.v1

8. Challenges, Limitations, and Future Directions Using Photoacoustic Imaging for Women's Health

Despite significant progress, several challenges remain for the widespread adoption of PAI in women's health applications. Limited optical penetration depth and signal attenuation in highly scattering biological tissues restrict imaging performance in deep pelvic organs, necessitating improved light-delivery strategies and optimized probe designs. Variability in imaging systems, reconstruction algorithms, and data formats also limits cross-study comparability, highlighting the need for standardized protocols and quantitative biomarkers. Motion artifacts, heterogeneous tissue composition, and safety constraints related to laser exposure further complicate clinical implementation, particularly in transvaginal and intraoperative settings. Future research should focus on developing miniaturized probe-based systems, multimodal integration with ultrasound and optical imaging, and using AI-assisted reconstruction and analysis to enhance sensitivity and diagnostic accuracy. Advances in targeted contrast agents, real-time imaging workflows, and regulatory standardization are expected to accelerate clinical translation, positioning PAI as a promising noninvasive tool for early diagnosis, disease-progression monitoring, and image-guided interventions in gynecological and reproductive health.

9. Conclusions

PAI has emerged as a powerful hybrid modality that bridges optical contrast with ultrasonic resolution, enabling noninvasive visualization of structural, functional, and molecular changes in biological tissues. Recent advances demonstrate the growing impact in women's health applications, including cervical assessment, ovarian lesion characterization, pregnancy monitoring, and evaluation of reproductive tissue remodeling. By providing label-free sensitivity to hemoglobin, collagen, water content, and vascular architecture, PAI offers unique diagnostic information that complements conventional imaging techniques such as ultrasound and MRI. The incorporation of targeted molecular probes has further enhanced its diagnostic sensitivity and expanded its theranostic potential for gynecological diseases. Moreover, the integration of PAI with clinically compatible platforms, together with advances in spectral imaging, artificial intelligence–assisted analysis, and probe-based systems, has accelerated its transition toward translational and clinical use.

Despite remaining challenges related to imaging depth, system standardization, and regulatory approval, ongoing technological innovations and collaborative standardization efforts are steadily addressing these limitations. Future progress will likely be driven by multimodal imaging integration, quantitative imaging biomarkers, targeted contrast agents, and workflow-compatible clinical devices. Collectively, these advancements position PAI as a promising next-generation tool for early disease detection, personalized diagnosis, and image-guided management in gynecological and reproductive medicine, with the potential to significantly improve clinical outcomes in women's health.

Funding: This research was funded by the National Institutes of Health (Grant R01HD108895).

Institutional Review Board Statement: Not applicable.

Informed Consent Statement: Not applicable.

Data Availability Statement: No new data were created or analyzed in this study.

Acknowledgments: The authors acknowledge the Department of Biomedical Engineering at Michigan State University.

Conflicts of Interest: The authors declare no conflicts of interest.

 doi:10.20944/preprints202603.1150.v1

References

1. He, X.; Su, J.; Wang, K.; Liang, Y.; Wang, L. Global, Regional, and National Prevalence and Trends of Gynecological Diseases among Women of Childbearing Age from 1990 to 2021: An Analysis of the Global Burden of Disease Study 2021. *PLoS One* **2025**, *20*, e0329336, doi:10.1371/journal.pone.0329336.
2. Gao, Y.; Wang, X.; Wang, Q.; Jiang, L.; Wu, C.; Guo, Y.; Cui, N.; Tang, H.; Tang, L. Rising Global Burden of Common Gynecological Diseases in Women of Childbearing Age from 1990 to 2021: An Update from the Global Burden of Disease Study 2021. *Reprod. Health* **2025**, *22*, 57, doi:10.1186/s12978-025-02013-1.
3. Hill, C.J.; Fakhreldin, M.; Maclean, A.; Dobson, L.; Nancarrow, L.; Bradfield, A.; Choi, F.; Daley, D.; Tempest, N.; Hapangama, D.K. Endometriosis and the Fallopian Tubes: Theories of Origin and Clinical Implications. *J. Clin. Med.* **2020**, *9*, 1905, doi:10.3390/jcm9061905.
4. Mikhaleva, L.M.; Radzinsky, V.E.; Orazov, M.R.; Khovanskaya, T.N.; Sorokina, A.V.; Mikhalev, S.A.; Volkova, S.V.; Shustova, V.B.; Sinelnikov, M.Y. Current Knowledge on Endometriosis Etiology: A Systematic Review of Literature. *IJWH* **2021**, *Volume 13*, 525–537, doi:10.2147/IJWH.S306135.
5. Pavaleanu, I.; Ana Balan, T.; Nicolae Poparlan, T.; Maria Haliciu, A.; Andrei Butureanu, T.; Maria Apetrei, A.; Socolov, R.; Ioana Pruteanu, A.; Anca Balan, R. Endometriosis-Associated Ovarian Carcinoma. In *Obstetrics and Gynecology*; Wu, W., Ju, R., Eds.; IntechOpen, 2024; Vol. 7 ISBN 978-0-85014-733-9.
6. Jayaprakasan, K.; Ojha, K. Diagnosis of Congenital Uterine Abnormalities: Practical Considerations. *J. Clin. Med.* **2022**, *11*, 1251, doi:10.3390/jcm11051251.
7. Dykes, T.M.; Siegel, C.; Dodson, W. Imaging of Congenital Uterine Anomalies: *Review and Self-Assessment Module*. *Am. J. Roentgenol.* **2007**, *189*, S1–S10, doi:10.2214/AJR.06.0821.
8. Sahu, S.A.; Shrivastava, D. A Comprehensive Review of Screening Methods for Ovarian Masses: Towards Earlier Detection. *Cureus* **2023**, doi:10.7759/cureus.48534.
9. Matsas, A.; Stefanoudakis, D.; Troupis, T.; Kontzoglou, K.; Eleftheriades, M.; Christopoulos, P.; Panoskaltsis, T.; Stamoula, E.; Iliopoulos, D.C. Tumor Markers and Their Diagnostic Significance in Ovarian Cancer. *Life* **2023**, *13*, 1689, doi:10.3390/life13081689.
10. Tsikouras, P.; Oikonomou, E.; Bothou, A.; Chaitidou, P.; Kyriakou, D.; Nikolettos, K.; Andreou, S.; Gaitatzi, F.; Nalbanti, T.; Peitsidis, P.; et al. The Impact of Endometriosis on Pregnancy. *J. Pers. Med.* **2024**, *14*, 126, doi:10.3390/jpm14010126.
11. Allaire, C.; Bedaiwy, M.A.; Yong, P.J. Diagnosis and Management of Endometriosis. *CMAJ* **2023**, *195*, E363–E371, doi:10.1503/cmaj.220637.
12. Napolitano, R.; Speltri, G.; Martini, P.; Porto, F.; Marvelli, L.; Niorettini, A.; Uccelli, L.; Urso, L.; Filippi, L.; Uslu, H.; et al. Molecular Imaging Advances in Endometriosis: The Promise of Radiopharmaceuticals. *Molecules* **2025**, *31*, 93, doi:10.3390/molecules31010093.
13. Scutelnicu, L.-A.; Luca, M.; Maftei, R. A Comparative Study on Endometriosis Automatic Diagnosis Using Magnetic Resonance Imaging and Ultrasound. *Hum. Centric Intell. Syst.* **2025**, *414*, 125-134. https://doi.org/10.1007/978-981-97-8598-8_12.
14. Sebastiano, J.; Rodriguez, C.; Samuels, Z.V.; Pepin, K.; Zeglis, B.M. Molecular Imaging in Gynecology: Beyond Cancer. *J. Nucl. Med.* **2024**, *65*, 998–1003, doi:10.2967/jnumed.124.267546.
15. Gaia-Oltean, A.I.; Boitor, D.; Pop, L.-A.; Galea, G.; Telecan, T.; Micu, R. Non-Invasive Methods for Early Diagnosis of Endometriosis—A Comprehensive Narrative Literature Review. *Healthcare* **2025**, *13*, 3276, doi:10.3390/healthcare13243276.
16. Kumar, P.P.P.; Chung, S.; Hadrick, K.; Hill, M.L.; Lee, M.; Kim, T.H.; Jeong, J.; Kim, T. Noninvasive Detection and Thermal Ablation Therapy of Endometriosis Using Silica-Coated Gold Nanorods. *Adv. Nanobiomed. Res.* **2025**, *5*, 2500101, doi:10.1002/anbr.202500101.
17. Xia, J.; Yao, J.; Wang, L.H.V. Photoacoustic Tomography: Principles and Advances. *PIER* **2014**, *147*, 1–22, doi:10.2528/PIER14032303.
18. Wang, L.V.; Hu, S. Photoacoustic Tomography: In Vivo Imaging from Organelles to Organs. *Science* **2012**, *335*, 1458–1462, doi:10.1126/science.1216210.
19. Yang, T.; Lou, Y.; Ying, Z. Nanoparticle-Ultrasound Synergy: An Emerging Theranostic Paradigm for Breast and Gynecologic Cancers. *Front. Oncol.* **2025**, *15*, 1617939, doi:10.3389/fonc.2025.1617939.

 doi:10.20944/preprints202603.1150.v1

20. Herrara, V.; Tarab-Ravski, D.; Chauhan, S.C.; Narang, N.; Mirazul Islam, M.; Peer, D.; Prasad, R.; Yallapu, M.M. Nanotechnology Strategies for Endometrium Health: Are We on the Right Track? *Bioact. Mater*. **2025**, *54*, 423–449, doi:10.1016/j.bioactmat.2025.08.016.
21. Peng, Y.; Zhang, M.; Yan, J.; Wang, R.; Xin, Y.; Zheng, X.; Zhu, L.; Fei, W.; Zhao, M. Emerging Bioengineering Breakthroughs in Precision Diagnosis and Therapy for Endometriosis and Adenomyosis. *J. Mater. Chem. B* **2025**, *13*, 742–762, doi:10.1039/D4TB01755B.
22. Xu, M.; Wang, L.V. Photoacoustic Imaging in Biomedicine. *Rev. Sci. Instrum.* **2006**, *77*, 041101, doi:10.1063/1.2195024.
23. Wang, L.V.; Yao, J. A Practical Guide to Photoacoustic Tomography in the Life Sciences. *Nat. Methods* **2016**, *13*, 627–638, doi:10.1038/nmeth.3925.
24. Yao, J.; Wang, L.V. Sensitivity of Photoacoustic Microscopy. *Photoacoustics* **2014**, *2*, 87–101, doi:10.1016/j.pacs.2014.04.002.
25. Upputuri, P.K.; Pramanik, M. Recent Advances in Photoacoustic Contrast Agents for in Vivo Imaging. *WIREs Nanomed. Nanobiotechnol.* **2020**, *12*, e1618, doi:10.1002/wnan.1618.
26. Han, S.; Lee, D.; Kim, S.; Kim, H.-H.; Jeong, S.; Kim, J. Contrast Agents for Photoacoustic Imaging: A Review Focusing on the Wavelength Range. *Biosensors* **2022**, *12*, 594, doi:10.3390/bios12080594.
27. Wang, L.; Zeng, W.; Long, K.; Chen, H.; Lan, R.; Liu, L.; Siok, W.T.; Wang, N. Advances in Photoacoustic Imaging Reconstruction and Quantitative Analysis for Biomedical Applications. *Vis. Comput. Ind. Biomed. Art* **2026**, *9*, 3, doi:10.1186/s42492-025-00213-x.
28. Yang, J.J.; Cho, S.-W.; Yao, J. Eavesdrop at Clinical Depths: Deep Photoacoustic Imaging with Internal Light Illumination. *Adv. Devices Instrum.* **2025**, *6*, 0100, doi:10.34133/adi.0100.
29. Park, J.; Choi, S.; Knieling, F.; Clingman, B.; Bohndiek, S.; Wang, L.V.; Kim, C. Clinical Translation of Photoacoustic Imaging. *Nat. Rev. Bioeng.* **2024**, *3*, 193–212, doi:10.1038/s44222-024-00240-y.
30. Merdasa, A.; Bunke, J.; Naumovska, M.; Albinsson, J.; Erlöv, T.; Cinthio, M.; Reistad, N.; Sheikh, R.; Malmsjö, M. Photoacoustic Imaging of the Spatial Distribution of Oxygen Saturation in an Ischemia-Reperfusion Model in Humans. *Biomed. Opt. Express* **2021**, *12*, 2484, doi:10.1364/BOE.418397.
31. Chen, J.; Xia, W. Photoacoustic Imaging: A Unique Imaging Examination for the Assessment of Diabetic Vascular Disease. *Front. Clin. Diabetes Healthc.* **2025**, *6*, 1651868, doi:10.3389/fcdhc.2025.1651868.
32. Mankovskii, G.; Hysi, E. Photoacoustic Imaging of Metabolic Activities across Biological Length Scales. *Physiology* **2025**, *40*, 224–232, doi:10.1152/physiol.00010.2024.
33. Dadkhah, A.; Jiao, S. Integrating Photoacoustic Microscopy with Other Imaging Technologies for Multimodal Imaging. *Exp. Biol. Med.* **2021**, *246*, 771–777, doi:10.1177/1535370220977176.
34. Defining the Clinical Niche for Photoacoustic Imaging. *Nat. Rev. Bioeng.* **2025**, *3*, 181–181, doi:10.1038/s44222-025-00284-8.
35. Lin, L.; Wang, L.V. The Emerging Role of Photoacoustic Imaging in Clinical Oncology. *Nat Rev Clin Oncol* **2022**, *19*, 365–384, doi:10.1038/s41571-022-00615-3.
36. Qiu, T.; Lan, Y.; Gao, W.; Zhou, M.; Liu, S.; Huang, W.; Zeng, S.; Pathak, J.L.; Yang, B.; Zhang, J. Photoacoustic Imaging as a Highly Efficient and Precise Imaging Strategy for the Evaluation of Brain Diseases. *Quant. Imaging Med. Surg.* **2021**, *11*, 2169–2186, doi:10.21037/qims-20-845.
37. Huang, C.; Zheng, E.; Zheng, W.; Zhang, H.; Cheng, Y.; Zhang, X.; Shijo, V.; Bing, R.W.; Komornicki, I.; Harris, L.M.; et al. Enhanced Clinical Photoacoustic Vascular Imaging through a Skin Localization Network and Adaptive Weighting. *Photoacoustics* **2025**, *42*, 100690, doi:10.1016/j.pacs.2025.100690.
38. Huang, M.; Yu, H.; Gao, R.; Liu, Y.; Zhou, X.; Fu, L.; Zhou, J.; Li, L. Photoacoustic Imaging in Inflammatory Orthopedic Diseases: Progress toward Precise Diagnostics and Predictive Regulation. *Adv. Sci.* **2025**, *12*, 2412745, doi:10.1002/advs.202412745.
39. Zhou, H.-C.; Chen, N.; Zhao, H.; Yin, T.; Zhang, J.; Zheng, W.; Song, L.; Liu, C.; Zheng, R. Optical-Resolution Photoacoustic Microscopy for Monitoring Vascular Normalization during Anti-Angiogenic Therapy. *Photoacoustics* **2019**, *15*, 100143, doi:10.1016/j.pacs.2019.100143.
40. Mantri, Y.; Tsujimoto, J.; Donovan, B.; Fernandes, C.C.; Garimella, P.S.; Penny, W.F.; Anderson, C.A.; Jokerst, J.V. Photoacoustic Monitoring of Angiogenesis Predicts Response to Therapy in Healing Wounds. *Wound Repair Regeneration* **2022**, *30*, 258–267, doi:10.1111/wrr.12992.

 doi:10.20944/preprints202603.1150.v1

41. Hu, S.; Wang, L.V. Photoacoustic Imaging and Characterization of the Microvasculature. *J. Biomed. Opt.* **2010**, *15*, 011101, doi:10.1117/1.3281673.
42. Sun, M.; Li, C.; Chen, N.; Zhao, H.; Ma, L.; Liu, C.; Shen, Y.; Lin, R.; Gong, X. Full Three-Dimensional Segmentation and Quantification of Tumor Vessels for Photoacoustic Images. *Photoacoustics* **2020**, *20*, 100212, doi:10.1016/j.pacs.2020.100212.
43. Wang, T.; Chen, J.; Nie, L.; Li, H. Photoacoustic Microscopy for Multiscale Biological System Visualization and Clinical Translation. *Adv. Sci.* **2026**, *13*, e21173, doi:10.1002/advs.202521173.
44. Hu, S.; Maslov, K.; Wang, L.V. Second-Generation Optical-Resolution Photoacoustic Microscopy with Improved Sensitivity and Speed. *Opt. Lett.* **2011**, *36*, 1134, doi:10.1364/OL.36.001134.
45. Maslov, K.; Zhang, H.F.; Hu, S.; Wang, L.V. Optical-Resolution Photoacoustic Microscopy for in Vivo Imaging of Single Capillaries. *Opt. Lett.* **2008**, *33*, 929, doi:10.1364/OL.33.000929.
46. Maslov, K.; Stoica, G.; Wang, L.V. In Vivo Dark-Field Reflection-Mode Photoacoustic Microscopy. *Opt. Lett.* **2005**, *30*, 625–627, doi:10.1364/ol.30.000625.
47. Xing, W.; Wang, L.; Maslov, K.; Wang, L.V. Integrated Optical- and Acoustic-Resolution Photoacoustic Microscopy Based on an Optical Fiber Bundle. *Opt. Lett.* **2013**, *38*, 52, doi:10.1364/OL.38.000052.
48. Laufer, J.; Norris, F.; Cleary, J.; Zhang, E.; Treeby, B.; Cox, B.; Johnson, P.; Scambler, P.; Lythgoe, M.; Beard, P. In Vivo Photoacoustic Imaging of Mouse Embryos. *J. Biomed. Opt.* **2012**, *17*, 061220, doi:10.1117/1.JBO.17.6.061220.
49. Xia, J.; Chatni, M.R.; Maslov, K.I.; Guo, Z.; Wang, K.; Anastasio, M.A.; Wang, L.V. Whole-Body Ring-Shaped Confocal Photoacoustic Computed Tomography of Small Animals in Vivo. *J. Biomed. Opt.* **2012**, *17*, 1, doi:10.1117/1.JBO.17.5.050506.
50. Xia, J.; Chen, W.; Maslov, K.I.; Anastasio, M.A.; Wang, L.V. Retrospective Respiration-Gated Whole-Body Photoacoustic Computed Tomography of Mice. *J. Biomed. Opt.* **2014**, *19*, 1, doi:10.1117/1.JBO.19.1.016003.
51. Kruger, R.A.; Kiser, W.L.; Reinecke, D.R.; Kruger, G.A.; Miller, K.D. Thermoacoustic Molecular Imaging of Small Animals. *Mol. Imaging* **2003**, *2*, 113–123, doi:10.1162/15353500200303109.
52. Brecht, H.-P.; Su, R.; Fronheiser, M.; Ermilov, S.A.; Conjusteau, A.; Oraevsky, A.A. Whole-Body Three-Dimensional Optoacoustic Tomography System for Small Animals. *J. Biomed. Opt.* **2009**, *14*, 064007, doi:10.1117/1.3259361.
53. Zhang, K.; Ge, N.; Shen, L.; Yang, F.; Qiu, J.; Guo, J.; Wang, K.; Wang, S.; Yang, F.; Sheng, S.; et al. Recent Research Progress of Photoacoustic Endoscopy in the Digestive System. *Endosc. Ultrasound* **2025**, *14*, 99–105, doi:10.1097/eus.0000000000000127.
54. Guo, H.; Li, Y.; Qi, W.; Xi, L. Photoacoustic Endoscopy: A Progress Review. *J. Biophotonics* **2020**, *13*, e202000217, doi:10.1002/jbio.202000217.
55. Liang, X.; Zhao, Y.; Li, L.; Sun, H.; Qin, W.; Li, T.; Guo, H.; Qi, W.; Xi, L. Multi-Scenario Photoacoustic Endoscopy for in Vivo Functional Imaging. *Photoacoustics* **2025**, *45*, 100750, doi:10.1016/j.pacs.2025.100750.
56. Kim, J.; Heo, D.; Cho, S.; Ha, M.; Park, J.; Ahn, J.; Kim, M.; Kim, D.; Jung, D.H.; Kim, H.H.; et al. Enhanced Dual-Mode Imaging: Superior Photoacoustic and Ultrasound Endoscopy in Live Pigs Using a Transparent Ultrasound Transducer. *Sci. Adv.* **2024**, *10*, eadq9960, doi:10.1126/sciadv.adq9960.
57. Zhu, Y.; Ni, L.; Hu, G.; Johnson, L.A.; Eaton, K.A.; Wang, X.; Higgins, P.D.R.; Xu, G. Prototype Endoscopic Photoacoustic-Ultrasound Balloon Catheter for Characterizing Intestinal Obstruction. *Biomed. Opt. Express* **2022**, *13*, 3355, doi:10.1364/BOE.456672.
58. Wen, X.; Lei, P.; Huang, S.; Chen, X.; Yuan, Y.; Ke, D.; Liu, R.; Liang, J.; Wang, E.; Wei, B.; et al. High-Fluence Relay-Based Disposable Photoacoustic-Ultrasonic Endoscopy for in Vivo Anatomical Imaging of Gastrointestinal Tract. *Photon. Res.* **2023**, *11*, 55, doi:10.1364/PRJ.470737.
59. Park, E.; Kim, D.; Ha, M.; Kim, D.; Kim, C. A Comprehensive Review of High-Performance Photoacoustic Microscopy Systems. *Photoacoustics* **2025**, *44*, 100739, doi:10.1016/j.pacs.2025.100739.
60. Choi, S.; Kim, J.; Jeon, H.; Kim, C.; Park, E.-Y. Advancements in Photoacoustic Detection Techniques for Biomedical Imaging. *npj Acoust.* **2025**, *1*, 1, doi:10.1038/s44384-025-00005-w.
61. Mallidi, S.; Luke, G.P.; Emelianov, S. Photoacoustic Imaging in Cancer Detection, Diagnosis, and Treatment Guidance. *Trends in Biotechnology* **2011**, *29*, 213–221, doi:10.1016/j.tibtech.2011.01.006.

 doi:10.20944/preprints202603.1150.v1

62. Lahoti, H.S.; Jogdand, S.D. Bioimaging: Evolution, Significance, and Deficit. *Cureus* **2022**, doi:10.7759/cureus.28923.
63. Varani, M.; Auletta, S.; Signore, A.; Galli, F. State of the Art of Natural Killer Cell Imaging: A Systematic Review. *Cancers* **2019**, *11*, 967, doi:10.3390/cancers11070967.
64. Wu, Y.; Huang, K.; Chen, G.; Lin, L. Advances in Photoacoustic Imaging of Breast Cancer. *Sensors* **2025**, *25*, 4812, doi:10.3390/s25154812.
65. Farajollahi, A.; Baharvand, M. Advancements in Photoacoustic Imaging for Cancer Diagnosis and Treatment. *Int. J. Pharm.* **2024**, *665*, 124736, doi:10.1016/j.ijpharm.2024.124736.
66. Park, B.; Oh, D.; Kim, J.; Kim, C. Functional Photoacoustic Imaging: From Nano- and Micro- to Macro-Scale. *Nano Convergence* **2023**, *10*, 29, doi:10.1186/s40580-023-00377-3.
67. Hill, M.L.; Chung, S.-J.; Woo, H.-J.; Park, C.R.; Hadrick, K.; Nafiujjaman, M.; Kumar, P.P.P.; Mwangi, L.; Parikh, R.; Kim, T. Exosome-Coated Prussian Blue Nanoparticles for Specific Targeting and Treatment of Glioblastoma. *ACS Appl. Mater. Interfaces* **2024**, acsami.4c02364, doi:10.1021/acsami.4c02364.
68. Yao, J.; Wang, L.V. Photoacoustic Brain Imaging: From Microscopic to Macroscopic Scales. *Neurophoton* **2014**, *1*, 011003, doi:10.1117/1.NPh.1.1.011003.
69. Xia, J.; Wang, L.V. Small-Animal Whole-Body Photoacoustic Tomography: A Review. *IEEE Trans. Biomed. Eng.* **2014**, *61*, 1380–1389, doi:10.1109/TBME.2013.2283507.
70. Kye, H.; Song, Y.; Ninjbadgar, T.; Kim, C.; Kim, J. Whole-Body Photoacoustic Imaging Techniques for Preclinical Small Animal Studies. *Sensors* **2022**, *22*, 5130, doi:10.3390/s22145130.
71. Wang, Z.; Yang, F.; Zhang, W.; Xiong, K.; Yang, S. Towards in Vivo Photoacoustic Human Imaging: Shining a New Light on Clinical Diagnostics. *Fundamental Research* **2024**, *4*, 1314–1330, doi:10.1016/j.fmre.2023.01.008.
72. Liu, H.; Wang, M.; Ji, F.; Jiang, Y.; Yang, M. Mini Review of Photoacoustic Clinical Imaging: A Noninvasive Tool for Disease Diagnosis and Treatment Evaluation. *J. Biomed. Opt.* **2024**, *29*, doi:10.1117/1.JBO.29.S1.S11522.
73. Yang, C.; Lan, H.; Gao, F.; Gao, F. Review of Deep Learning for Photoacoustic Imaging. *Photoacoustics* **2021**, *21*, 100215, doi:10.1016/j.pacs.2020.100215.
74. Deng, H.; Qiao, H.; Dai, Q.; Ma, C. Deep Learning in Photoacoustic Imaging: A Review. *J. Biomed. Opt.* **2021**, *26*, doi:10.1117/1.JBO.26.4.040901.
75. Tsang, V.T.C.; Li, X.; Wong, T.T.W. A Review of Endogenous and Exogenous Contrast Agents Used in Photoacoustic Tomography with Different Sensing Configurations. *Sensors* **2020**, *20*, 5595, doi:10.3390/s20195595.
76. Wu, C.; Zuo, H.; Cui, M.; Deng, H.; Chen, Y.; Wang, X.; Wang, B.; Ma, C. Blood Oxygenation Quantification in Multispectral Photoacoustic Tomography Using a Convex Cone Approach. *IEEE Trans. Med. Imaging* **2025**, *44*, 2842–2853, doi:10.1109/TMI.2025.3551744.
77. Lin, C.-L.; Wu, M.-H.; Ho, Y.-H.; Lin, F.-Y.; Lu, Y.-H.; Hsueh, Y.-Y.; Chen, C.-C. Multispectral Imaging-Based System for Detecting Tissue Oxygen Saturation With Wound Segmentation for Monitoring Wound Healing. *IEEE J. Transl. Eng. Health Med.* **2024**, *12*, 468–479, doi:10.1109/JTEHM.2024.3399232.
78. Deán-Ben, X.L.; Gottschalk, S.; Mc Larney, B.; Shoham, S.; Razansky, D. Advanced Optoacoustic Methods for Multiscale Imaging of in Vivo Dynamics. *Chem. Soc. Rev.* **2017**, *46*, 2158–2198, doi:10.1039/C6CS00765A.
79. John, S.; Hester, S.; Basij, M.; Paul, A.; Xavierselvan, M.; Mehrmohammadi, M.; Mallidi, S. Niche Preclinical and Clinical Applications of Photoacoustic Imaging with Endogenous Contrast. *Photoacoustics* **2023**, *32*, 100533, doi:10.1016/j.pacs.2023.100533.
80. Haedicke, K.; Agemy, L.; Omar, M.; Berezhnoi, A.; Roberts, S.; Longo-Machado, C.; Skubal, M.; Nagar, K.; Hsu, H.-T.; Kim, K.; et al. High-Resolution Optoacoustic Imaging of Tissue Responses to Vascular-Targeted Therapies. *Nat. Biomed. Eng.* **2020**, *4*, 286–297, doi:10.1038/s41551-020-0527-8.
81. Yamaleyeva, L.M.; Sun, Y.; Bledsoe, T.; Hoke, A.; Gurley, S.B.; Brosnihan, K.B. Photoacoustic Imaging for *in Vivo* Quantification of Placental Oxygenation in Mice. *The FASEB Journal* **2017**, *31*, 5520–5529, doi:10.1096/fj.201700047RR.
82. Nasri, D.; Manwar, R.; Kaushik, A.; Er, E.E.; Avanaki, K. Photoacoustic Imaging for Investigating Tumor Hypoxia: A Strategic Assessment. *Theranostics* **2023**, *13*, 3346–3367, doi:10.7150/thno.84253.

 doi:10.20944/preprints202603.1150.v1

83. Shrestha, B.; DeLuna, F.; Anastasio, M.A.; Yong Ye, J.; Brey, E.M. Photoacoustic Imaging in Tissue Engineering and Regenerative Medicine. *Tissue Engineering Part B: Reviews* **2020**, *26*, 79–102, doi:10.1089/ten.teb.2019.0296.
84. Yang, X.; Chen, Y.-H.; Xia, F.; Sawan, M. Photoacoustic Imaging for Monitoring of Stroke Diseases: A Review. *Photoacoustics* **2021**, *23*, 100287, doi:10.1016/j.pacs.2021.100287.
85. Bodea, S.-V.; Westmeyer, G.G. Photoacoustic Neuroimaging - Perspectives on a Maturing Imaging Technique and Its Applications in Neuroscience. *Front. Neurosci.* **2021**, *15*, 655247, doi:10.3389/fnins.2021.655247.
86. Matsumoto, Y.; Asao, Y.; Yoshikawa, A.; Sekiguchi, H.; Takada, M.; Furu, M.; Saito, S.; Kataoka, M.; Abe, H.; Yagi, T.; et al. Label-Free Photoacoustic Imaging of Human Palmar Vessels: A Structural Morphological Analysis. *Sci. Rep.* **2018**, *8*, 786, doi:10.1038/s41598-018-19161-z.
87. He, Y.; Shi, J.; Maslov, K.I.; Cao, R.; Wang, L.V. Wave of Single-Impulse-Stimulated Fast Initial Dip in Single Vessels of Mouse Brains Imaged by High-Speed Functional Photoacoustic Microscopy. *J. Biomed. Opt.* **2020**, *25*, 1, doi:10.1117/1.JBO.25.6.066501.
88. Lin, L.; Hu, P.; Shi, J.; Appleton, C.M.; Maslov, K.; Li, L.; Zhang, R.; Wang, L.V. Single-Breath-Hold Photoacoustic Computed Tomography of the Breast. *Nat. Commun.* **2018**, *9*, 2352, doi:10.1038/s41467-018-04576-z.
89. Zhang, H.F.; Maslov, K.; Stoica, G.; Wang, L.V. Functional Photoacoustic Microscopy for High-Resolution and Noninvasive in Vivo Imaging. *Nat. Biotechnol.* **2006**, *24*, 848–851, doi:10.1038/nbt1220.
90. Rich, L.J.; Seshadri, M. Photoacoustic Imaging of Vascular Hemodynamics: Validation with Blood Oxygenation Level–Dependent MR Imaging. *Radiology* **2015**, *275*, 110–118, doi:10.1148/radiol.14140654.
91. Gargiulo, S.; Albanese, S.; Mancini, M. State-of-the-Art Preclinical Photoacoustic Imaging in Oncology: Recent Advances in Cancer Theranostics. *Contrast Media Mol Imaging* **2019**, *2019*, 5080267, doi:10.1155/2019/5080267.
92. Ying, Y.; Zhang, H.; Lin, L. Photoacoustic Imaging of Human Skin for Accurate Diagnosis and Treatment Guidance. *Optics* **2024**, *5*, 133–150, doi:10.3390/opt5010010.
93. Silverman, R.H.; Kong, F.; Chen, Y.C.; Lloyd, H.O.; Kim, H.H.; Cannata, J.M.; Shung, K.K.; Coleman, D.J. High-Resolution Photoacoustic Imaging of Ocular Tissues. *Ultrasound in Medicine & Biology* **2010**, *36*, 733–742, doi:10.1016/j.ultrasmedbio.2010.02.006.
94. Shu, X.; Li, H.; Dong, B.; Sun, C.; Zhang, H.F. Quantifying Melanin Concentration in Retinal Pigment Epithelium Using Broadband Photoacoustic Microscopy. *Biomed. Opt. Express* **2017**, *8*, 2851, doi:10.1364/BOE.8.002851.
95. Shu, X.; Liu, W.; Zhang, H.F. Monte Carlo Investigation on Quantifying the Retinal Pigment Epithelium Melanin Concentration by Photoacoustic Ophthalmoscopy. *J. Biomed. Opt* **2015**, *20*, 106005, doi:10.1117/1.JBO.20.10.106005.
96. Fakhoury, J.W.; Lara, J.B.; Manwar, R.; Zafar, M.; Xu, Q.; Engel, R.; Tsoukas, M.M.; Daveluy, S.; Mehregan, D.; Avanaki, K. Photoacoustic Imaging for Cutaneous Melanoma Assessment: A Comprehensive Review. *J. Biomed. Opt.* **2024**, *29*, doi:10.1117/1.JBO.29.S1.S11518.
97. Langhout, G.C.; Grootendorst, D.J.; Nieweg, O.E.; Wouters, M.W.J.M.; Van Der Hage, J.A.; Jose, J.; Van Boven, H.; Steenbergen, W.; Manohar, S.; Ruers, T.J.M. Detection of Melanoma Metastases in Resected Human Lymph Nodes by Noninvasive Multispectral Photoacoustic Imaging. *Int. J. Biomed. Imaging.* **2014**, *2014*, 1–7, doi:10.1155/2014/163652.
98. Farooq, A.; Sabah, S.; Dhou, S.; Alsawaftah, N.; Husseini, G. Exogenous Contrast Agents in Photoacoustic Imaging: An In Vivo Review for Tumor Imaging. *Nanomater.* **2022**, *12*, 393, doi:10.3390/nano12030393.
99. Lemaster, J.E.; Jokerst, J.V. What Is New in Nanoparticle-based Photoacoustic Imaging? *WIREs Nanomed Nanobiotechnol* **2017**, *9*, e1404, doi:10.1002/wnan.1404.
100. Beziere, N.; Lozano, N.; Nunes, A.; Salichs, J.; Queiros, D.; Kostarelos, K.; Ntziachristos, V. Dynamic Imaging of PEGylated Indocyanine Green (ICG) Liposomes within the Tumor Microenvironment Using Multi-Spectral Optoacoustic Tomography (MSOT). *Biomaterials* **2015**, *37*, 415–424, doi:10.1016/j.biomaterials.2014.10.014.

 doi:10.20944/preprints202603.1150.v1

101. Bam, R.; Laffey, M.; Nottberg, K.; Lown, P.S.; Hackel, B.J.; Wilson, K.E. Affibody-Indocyanine Green Based Contrast Agent for Photoacoustic and Fluorescence Molecular Imaging of B7–H3 Expression in Breast Cancer. *Bioconjugate Chem.* **2019**, *30*, 1677–1689, doi:10.1021/acs.bioconjchem.9b00239.
102. Rahman, M.S.; Hadrick, K.; Chung, S.-J.; Carley, I.; Yoo, J.-Y.; Nahar, S.; Kim, T.H.; Kim, T.; Jeong, J.-W. Nanoceria as a Non-Steroidal Anti-Inflammatory Drug for Endometriosis Theranostics. *J. Contr. Release* **2025**, *378*, 1015–1029, doi:10.1016/j.jconrel.2024.12.074.
103. Wang, J.; Lin, C.-Y.; Moore, C.; Jhunjhunwala, A.; Jokerst, J.V. Switchable Photoacoustic Intensity of Methylene Blue via Sodium Dodecyl Sulfate Micellization. *Langmuir* **2018**, *34*, 359–365, doi:10.1021/acs.langmuir.7b03718.
104. Jeevarathinam, A.S.; Lemaster, J.E.; Chen, F.; Zhao, E.; Jokerst, J.V. Photoacoustic Imaging Quantifies Drug Release from Nanocarriers via Redox Chemistry of Dye-Labeled Cargo. *Angew. Chem. Int. Ed.* **2020**, *59*, 4678–4683, doi:10.1002/anie.201914120.
105. Pilatou, M.C.; Marani, E.; De Mul, F.F.M.; Steenbergen, W. Photoacoustic Imaging of Brain Perfusion on Albino Rats by Using Evans Blue as Contrast Agent. *Archives of Physiology and Biochemistry* **2003**, *111*, 389–397, doi:10.3109/13813450312331337649.
106. Yao, J.; Maslov, K.I.; Hu, S.; Wang, L.V. Evans Blue Dye-Enhanced Capillary-Resolution Photoacoustic Microscopy in Vivo. *J. Biomed. Opt.* **2009**, *14*, 1, doi:10.1117/1.3251044.
107. Morales, J.; Pawle, R.H.; Akkilic, N.; Luo, Y.; Xavierselvan, M.; Albokhari, R.; Calderon, I.A.C.; Selfridge, S.; Minns, R.; Takiff, L.; et al. DNA-Based Photoacoustic Nanosensor for Interferon Gamma Detection. *ACS Sens.* **2019**, *4*, 1313–1322, doi:10.1021/acssensors.9b00209.
108. Liu, S.; Zhou, X.; Zhang, H.; Ou, H.; Lam, J.W.Y.; Liu, Y.; Shi, L.; Ding, D.; Tang, B.Z. Molecular Motion in Aggregates: Manipulating TICT for Boosting Photothermal Theranostics. *J. Am. Chem. Soc.* **2019**, *141*, 5359–5368, doi:10.1021/jacs.8b13889.
109. Xu, M.; Sun, Q.; Wang, X.; Gao, H.; Liu, Z. Near-Infrared Absorbing BODIPY-Xanthene Hybrids for Multiplexed Photoacoustic Imaging. *Org. Lett.* **2024**, *26*, 3750–3755, doi:10.1021/acs.orglett.4c00842.
110. Fan, Q.; Cheng, K.; Yang, Z.; Zhang, R.; Yang, M.; Hu, X.; Ma, X.; Bu, L.; Lu, X.; Xiong, X.; et al. Perylene-Diimide-Based Nanoparticles as Highly Efficient Photoacoustic Agents for Deep Brain Tumor Imaging in Living Mice. *Adv. Mater.* **2015**, *27*, 843–847, doi:10.1002/adma.201402972.
111. Li, H.; Yue, L.; Li, L.; Liu, G.; Zhang, J.; Luo, X.; Wu, F. Triphenylamine-Perylene Diimide Conjugate-Based Organic Nanoparticles for Photoacoustic Imaging and Cancer Phototherapy. *Colloids and Surfaces B: Biointerfaces* **2021**, *205*, 111841, doi:10.1016/j.colsurfb.2021.111841.
112. Kim, K.; Huang, S.-W.; Ashkenazi, S.; O'Donnell, M.; Agarwal, A.; Kotov, N.A.; Denny, M.F.; Kaplan, M.J. Photoacoustic Imaging of Early Inflammatory Response Using Gold Nanorods. *Appl. Phys. Lett.* **2007**, *90*, 223901, doi:10.1063/1.2743752.
113. Li, W.; Chen, X. Gold Nanoparticles for Photoacoustic Imaging. *Nanomedicine (Lond.)* **2015**, *10*, 299–320, doi:10.2217/nnm.14.169.
114. Chen, Y.-S.; Zhao, Y.; Yoon, S.J.; Gambhir, S.S.; Emelianov, S. Miniature Gold Nanorods for Photoacoustic Molecular Imaging in the Second Near-Infrared Optical Window. *Nat. Nanotechnol.* **2019**, *14*, 465–472, doi:10.1038/s41565-019-0392-3.
115. Wang, B.; Joshi, P.; Sapozhnikova, V.; Amirian, J.; Litovsky, S.H.; Smalling, R.; Sokolov, K.; Emelianov, S. Intravascular Photoacoustic Imaging of Macrophages Using Molecularly Targeted Gold Nanoparticles.; Oraevsky, A.A., Wang, L.V., Eds.; San Francisco, California, February 11 2010; p. 75640A.
116. Cheheltani, R.; Ezzibdeh, R.M.; Chhour, P.; Pulaparthi, K.; Kim, J.; Jurcova, M.; Hsu, J.C.; Blundell, C.; Litt, H.I.; Ferrari, V.A.; et al. Tunable, Biodegradable Gold Nanoparticles as Contrast Agents for Computed Tomography and Photoacoustic Imaging. *Biomaterials* **2016**, *102*, 87–97, doi:10.1016/j.biomaterials.2016.06.015.
117. Kim, T.; Zhang, Q.; Li, J.; Zhang, L.; Jokerst, J.V. A Gold/Silver Hybrid Nanoparticle for Treatment and Photoacoustic Imaging of Bacterial Infection. *ACS Nano* **2018**, *12*, 5615–5625, doi:10.1021/acsnano.8b01362.
118. Dumani, D.S.; Cook, J.R.; Kubelick, K.P.; Luci, J.J.; Emelianov, S.Y. Photomagnetic Prussian Blue Nanocubes: Synthesis, Characterization, and Biomedical Applications. *Nanomedicine: Nanotechnology, Biology and Medicine* **2020**, *24*, 102138, doi:10.1016/j.nano.2019.102138.

 doi:10.20944/preprints202603.1150.v1

119. Fu, G.; Liu, W.; Feng, S.; Yue, X. Prussian Blue Nanoparticles Operate as a New Generation of Photothermal Ablation Agents for Cancer Therapy. *Chem. Commun.* **2012**, *48*, 11567, doi:10.1039/c2cc36456e.
120. Kim, M.; VanderLaan, D.; Lee, J.; Choe, A.; Kubelick, K.P.; Kim, J.; Emelianov, S.Y. Hyper-Branched Gold Nanoconstructs for Photoacoustic Imaging in the Near-Infrared Optical Window. *Nano Lett.* **2023**, *23*, 9257–9265, doi:10.1021/acs.nanolett.3c02177.
121. Kumar, P.P.P.; Lim, D.-K. Photothermal Effect of Gold Nanoparticles as a Nanomedicine for Diagnosis and Therapeutics. *Pharmaceutics* **2023**, *15*, 2349, doi:10.3390/pharmaceutics15092349.
122. Yim, W.; Borum, R.M.; Zhou, J.; Mantri, Y.; Wu, Z.; Zhou, J.; Jin, Z.; Creyer, M.; Jokerst, J.V. Ultrasmall Gold Nanorod-Polydopamine Hybrids for Enhanced Photoacoustic Imaging and Photothermal Therapy in Second near-Infrared Window. *Nanotheranostics* **2022**, *6*, 79–90, doi:10.7150/ntno.63634.
123. Sun, I.-C.; Emelianov, S. Gas-Generating Nanoparticles for Contrast-Enhanced Ultrasound Imaging. *Nanoscale* **2019**, *11*, 16235–16240, doi:10.1039/C9NR04471J.
124. Jokerst, J.V.; Cole, A.J.; Van De Sompel, D.; Gambhir, S.S. Gold Nanorods for Ovarian Cancer Detection with Photoacoustic Imaging and Resection Guidance *via* Raman Imaging in Living Mice. *ACS Nano* **2012**, *6*, 10366–10377, doi:10.1021/nn304347g.
125. Liu, Y.; He, J.; Yang, K.; Yi, C.; Liu, Y.; Nie, L.; Khashab, N.M.; Chen, X.; Nie, Z. Folding Up of Gold Nanoparticle Strings into Plasmonic Vesicles for Enhanced Photoacoustic Imaging. *Angew. Chem. Int. Ed.* **2015**, *54*, 15809–15812, doi:10.1002/anie.201508616.
126. Lee, S.; Lee, D.; Kim, C. Photoacoustic Imaging with Carbon Nanomaterials. In *Carbon Nanomaterials for Bioimaging, Bioanalysis, and Therapy*; Hui, Y.Y., Chang, H., Dong, H., Zhang, X., Eds.; Wiley, 2019; pp. 139–166 ISBN 978-1-119-37345-2.
127. Zerda, A.D.L.; Liu, Z.; Bodapati, S.; Teed, R.; Vaithilingam, S.; Khuri-Yakub, B.T.; Chen, X.; Dai, H.; Gambhir, S.S. Ultrahigh Sensitivity Carbon Nanotube Agents for Photoacoustic Molecular Imaging in Living Mice. *Nano Lett.* **2010**, *10*, 2168–2172, doi:10.1021/nl100890d.
128. Jeong, S.; Yoo, S.W.; Kim, H.J.; Park, J.; Kim, J.W.; Lee, C.; Kim, H. Recent Progress on Molecular Photoacoustic Imaging with Carbon-Based Nanocomposites. *Materials* **2021**, *14*, 5643, doi:10.3390/ma14195643.
129. Lee, I.-Y.S.; Hayama, Y.; Suzuki, H.; Osawa, T. Photoacoustic Sensitization and Laser-Induced Cavitation in Polymer Solutions by Carbon Nanotubes. *J. Phys. Chem. C* **2010**, *114*, 22392–22397, doi:10.1021/jp105524h.
130. Kim, J.-W.; Galanzha, E.I.; Shashkov, E.V.; Moon, H.-M.; Zharov, V.P. Golden Carbon Nanotubes as Multimodal Photoacoustic and Photothermal High-Contrast Molecular Agents. *Nat. Nanotech.* **2009**, *4*, 688–694, doi:10.1038/nnano.2009.231.
131. Xiang, L.; Yuan, Y.; Xing, D.; Ou, Z.; Yang, S.; Zhou, F. Photoacoustic Molecular Imaging with Antibody-Functionalized Single-Walled Carbon Nanotubes for Early Diagnosis of Tumor. *J. Biomed. Opt.* **2009**, *14*, 021008, doi:10.1117/1.3078809.
132. Xiang, L.; Xing, D.; Yuan, Y.; Huang, L. In Vivo Photoacoustic Molecular Imaging with Targeting Single-Walled Carbon Nanotubes.; Luo, Q., Wang, L.V., Tuchin, V.V., Eds.; Wuhan, China, December 11 2008; p. 728010.
133. Zanganeh, S.; Aguirre, A.; Biswal, N.C.; Pavlik, C.; Smith, M.B.; Alqasemi, U.; Li, H.; Zhu, Q. Hypoxia Targeted Carbon Nanotubes as a Sensitive Contrast Agent for Photoacoustic Imaging of Tumors.; Oraevsky, A.A., Wang, L.V., Eds.; San Francisco, California, USA, February 10 2011; p. 78991S.
134. Gifani, M.; Eddins, D.J.; Kosuge, H.; Zhang, Y.; Paluri, S.L.A.; Larson, T.; Leeper, N.; Herzenberg, L.A.; Gambhir, S.S.; McConnell, M.V.; et al. Ultraselective Carbon Nanotubes for Photoacoustic Imaging of Inflamed Atherosclerotic Plaques (Adv. Funct. Mater. 37/2021). *Adv Funct Materials* **2021**, *31*, 2170271, doi:10.1002/adfm.202170271.
135. Wang, C.; Bao, C.; Liang, S.; Fu, H.; Wang, K.; Deng, M.; Liao, Q.; Cui, D. RGD-Conjugated Silica-Coated Gold Nanorods on the Surface of Carbon Nanotubes for Targeted Photoacoustic Imaging of Gastric Cancer. *Nanoscale Res. Lett.* **2014**, *9*, 264, doi:10.1186/1556-276X-9-264.
136. Koo, J.; Jeon, M.; Oh, Y.; Kang, H.W.; Kim, J.; Kim, C.; Oh, J. *In Vivo* Non-Ionizing Photoacoustic Mapping of Sentinel Lymph Nodes and Bladders with ICG-Enhanced Carbon Nanotubes. *Phys. Med. Biol.* **2012**, *57*, 7853–7862, doi:10.1088/0031-9155/57/23/7853.

 doi:10.20944/preprints202603.1150.v1

137. Kumar, P.P.P. Organic Dyes for Light-Based Biomedical Imaging and Therapy 2026.
138. Li, C.; Liu, C.; Fan, Y.; Ma, X.; Zhan, Y.; Lu, X.; Sun, Y. Recent Development of Near-Infrared Photoacoustic Probes Based on Small-Molecule Organic Dye. *RSC Chem. Biol.* **2021**, *2*, 743–758, doi:10.1039/D0CB00225A.
139. Song, K.H.; Stein, E.W.; Margenthaler, J.A.; Wang, L.V. Noninvasive Photoacoustic Identification of Sentinel Lymph Nodes Containing Methylene Blue in Vivo in a Rat Model. *J. Biomed. Opt.* **2008**, *13*, 054033, doi:10.1117/1.2976427.
140. Song, L.; Kim, C.; Maslov, K.; Shung, K.K.; Wang, L.V. High-Speed Dynamic 3D Photoacoustic Imaging of Sentinel Lymph Node in a Murine Model Using an Ultrasound Array: Dynamic 3D Photoacoustic Imaging of Sentinel Lymph Node. *Med. Phys.* **2009**, *36*, 3724–3729, doi:10.1118/1.3168598.
141. Jeon, M.; Song, W.; Huynh, E.; Kim, J.; Kim, J.; Helfield, B.L.; Leung, B.Y.C.; Goertz, D.E.; Zheng, G.; Oh, J.; et al. Methylene Blue Microbubbles as a Model Dual-Modality Contrast Agent for Ultrasound and Activatable Photoacoustic Imaging. *J. Biomed. Opt* **2014**, *19*, 016005, doi:10.1117/1.JBO.19.1.016005.
142. Hartono, M.; Baker, A.G.; Else, T.R.; Evtushenko, A.S.; Bohndiek, S.E.; Muñoz-Espín, D.; Fruk, L. Photoacoustic Polydopamine-Indocyanine Green (PDA-ICG) Nanoprobe for Detection of Senescent Cells. *Sci. Rep.* **2024**, *14*, 29506, doi:10.1038/s41598-024-79667-7.
143. Ador, T.; Fournié, M.; Rigollet, S.; Counil, C.; Stupar, V.; Barbier, E.L.; Pichon, C.; Delalande, A. Ultrasound-Assisted Blood–Brain Barrier Opening Monitoring by Photoacoustic and Fluorescence Imaging Using Indocyanine Green. *Ultrasound in Medicine & Biology* **2025**, *51*, 1059–1069, doi:10.1016/j.ultrasmedbio.2025.02.016.
144. Kim, C.; Song, K.H.; Gao, F.; Wang, L.V. Sentinel Lymph Nodes and Lymphatic Vessels: Noninvasive Dual-Modality in Vivo Mapping by Using Indocyanine Green in Rats—Volumetric Spectroscopic Photoacoustic Imaging and Planar Fluorescence Imaging. *Radiology* **2010**, *255*, 442–450, doi:10.1148/radiol.10090281.
145. Miao, Q.; Lyu, Y.; Ding, D.; Pu, K. Semiconducting Oligomer Nanoparticles as an Activatable Photoacoustic Probe with Amplified Brightness for In Vivo Imaging of pH. *Advanced Materials* **2016**, *28*, 3662–3668, doi:10.1002/adma.201505681.
146. Reinhardt, C.J.; Zhou, E.Y.; Jorgensen, M.D.; Partipilo, G.; Chan, J. A Ratiometric Acoustogenic Probe for *in Vivo* Imaging of Endogenous Nitric Oxide. *J. Am. Chem. Soc.* **2018**, *140*, 1011–1018, doi:10.1021/jacs.7b10783.
147. Park, E.-Y.; Oh, D.; Park, S.; Kim, W.; Kim, C. New Contrast Agents for Photoacoustic Imaging and Theranostics: Recent 5-Year Overview on Phthalocyanine/Naphthalocyanine-Based Nanoparticles. *APL Bioeng.* **2021**, *5*, 031510, doi:10.1063/5.0047660.
148. Zhang, Y.; Jeon, M.; Rich, L.J.; Hong, H.; Geng, J.; Zhang, Y.; Shi, S.; Barnhart, T.E.; Alexandridis, P.; Huizinga, J.D.; et al. Non-Invasive Multimodal Functional Imaging of the Intestine with Frozen Micellar Naphthalocyanines. *Nature Nanotech.* **2014**, *9*, 631–638, doi:10.1038/nnano.2014.130.
149. Lee, C.; Kim, J.; Zhang, Y.; Jeon, M.; Liu, C.; Song, L.; Lovell, J.F.; Kim, C. Dual-Color Photoacoustic Lymph Node Imaging Using Nanoformulated Naphthalocyanines. *Biomaterials* **2015**, *73*, 142–148, doi:10.1016/j.biomaterials.2015.09.023.
150. Zhang, Y.; Hong, H.; Sun, B.; Carter, K.; Qin, Y.; Wei, W.; Wang, D.; Jeon, M.; Geng, J.; Nickles, R.J.; et al. Surfactant-Stripped Naphthalocyanines for Multimodal Tumor Theranostics with Upconversion Guidance Cream. *Nanoscale* **2017**, *9*, 3391–3398, doi:10.1039/C6NR09321C.
151. Choi, H.; Choi, W.; Kim, J.; Kong, W.H.; Kim, K.S.; Kim, C.; Hahn, S.K. Multifunctional Nanodroplets Encapsulating Naphthalocyanine and Perfluorohexane for Bimodal Image-Guided Therapy. *Biomacromolecules* **2019**, *20*, 3767–3777, doi:10.1021/acs.biomac.9b00842.
152. Jiang, Y.; Upputuri, P.K.; Xie, C.; Lyu, Y.; Zhang, L.; Xiong, Q.; Pramanik, M.; Pu, K. Broadband Absorbing Semiconducting Polymer Nanoparticles for Photoacoustic Imaging in Second Near-Infrared Window. *Nano Lett.* **2017**, *17*, 4964–4969, doi:10.1021/acs.nanolett.7b02106.
153. Jiang, Y.; Upputuri, P.K.; Xie, C.; Zeng, Z.; Sharma, A.; Zhen, X.; Li, J.; Huang, J.; Pramanik, M.; Pu, K. Metabolizable Semiconducting Polymer Nanoparticles for Second Near-Infrared Photoacoustic Imaging. *Adv. Mater.* **2019**, *31*, 1808166, doi:10.1002/adma.201808166.
154. Zhang, W.; Sun, X.; Huang, T.; Pan, X.; Sun, P.; Li, J.; Zhang, H.; Lu, X.; Fan, Q.; Huang, W. 1300 Nm Absorption Two-Acceptor Semiconducting Polymer Nanoparticles for NIR-II Photoacoustic Imaging

 doi:10.20944/preprints202603.1150.v1

System Guided NIR-II Photothermal Therapy. *Chem. Commun.* **2019**, *55*, 9487–9490, doi:10.1039/C9CC04196F.

155. Guo, B.; Chen, J.; Chen, N.; Middha, E.; Xu, S.; Pan, Y.; Wu, M.; Li, K.; Liu, C.; Liu, B. High-Resolution 3D NIR-II Photoacoustic Imaging of Cerebral and Tumor Vasculatures Using Conjugated Polymer Nanoparticles as Contrast Agent. *Adv. Mater.* **2019**, *31*, 1808355, doi:10.1002/adma.201808355.
156. Yang, E.; Khaled, A.; Liang, X.; De La Cerda, J.; Schuler, F.W.; Goel, S.; Pagel, M.D. Evaluations of a Cutaneous Wound Healing Model Using Oxygen Enhanced – Dynamic Contrast Enhanced Photoacoustic Imaging (OE-DCE PAI). *Mol. Imaging Biol.* **2024**, *26*, 995–1004, doi:10.1007/s11307-024-01966-2.
157. Chen, Y.-S.; Yoon, S.J.; Frey, W.; Dockery, M.; Emelianov, S. Dynamic Contrast-Enhanced Photoacoustic Imaging Using Photothermal Stimuli-Responsive Composite Nanomodulators. *Nat. Commun.* **2017**, *8*, 15782, doi:10.1038/ncomms15782.
158. Zoń, A.; Bednarek, I. Cisplatin in Ovarian Cancer Treatment—Known Limitations in Therapy Force New Solutions. *Int. J. Mol. Sci* . **2023**, *24*, 7585, doi:10.3390/ijms24087585.
159. Garg, P.; Krishna, M.; Subbalakshmi, A.R.; Ramisetty, S.; Mohanty, A.; Kulkarni, P.; Horne, D.; Salgia, R.; Singhal, S.S. Emerging Biomarkers and Molecular Targets for Precision Medicine in Cervical Cancer. *Biochimica et Biophysica Acta (BBA) - Reviews on Cancer* **2024**, *1879*, 189106, doi:10.1016/j.bbcan.2024.189106.
160. Ding, Q.; Guo, A.; Zhang, S.; Gu, C.; Wang, X.; Li, X.; Gu, M.; Kim, J.S. Phototheranostics: An Advanced Approach for Precise Diagnosis and Treatment of Gynecological Inflammation and Tumors. *Biomaterials* **2025**, *316*, 123012, doi:10.1016/j.biomaterials.2024.123012.
161. Christie, E.L.; Bowtell, D.D.L. Acquired Chemotherapy Resistance in Ovarian Cancer. *Annals of Oncology* **2017**, *28*, viii13–viii15, doi:10.1093/annonc/mdx446.
162. Chendian, T.; Guohua, H.; Wang, Z.; Fang, L.; Luo, S.; Liu, X.; Shi, Q. Factors Associated with Thermal Injury of Abdominal Skin in Focused Ultrasound Ablation of Uterine Fibroids. *Int. J. Hyperthermia* **2024**, *41*, 2295232, doi:10.1080/02656736.2023.2295232.
163. Liu, X.; Liu, G.; Mao, Y.; Luo, J.; Cao, Y.; Tan, W.; Li, W.; Yu, H.; Jia, X.; Li, H. Engineering Extracellular Vesicles Mimetics for Targeted Chemotherapy of Drug-Resistant Ovary Cancer. *Nanomedicine (Lond.)* **2024**, *19*, 25–41, doi:10.2217/nnm-2023-0289.
164. Jiang, Y.; Huang, S.; Zhang, L.; Zhou, Y.; Zhang, W.; Wan, T.; Gu, H.; Ouyang, Y.; Zheng, X.; Liu, P.; et al. Targeting the Cdc2-like kinase 2 for overcoming platinum resistance in ovarian cancer. *MedComm* **2024**, *5*, e537, doi:10.1002/mco2.537.
165. Spence, T.; De Souza, R.; Dou, Y.; Stapleton, S.; Reilly, R.M.; Allen, C. Integration of Imaging into Clinical Practice to Assess the Delivery and Performance of Macromolecular and Nanotechnology-Based Oncology Therapies. *J. Control. Release* **2015**, *219*, 295–312, doi:10.1016/j.jconrel.2015.09.036.
166. Dong, H.; Tang, R.; Hu, Y.; Zhong, S.; Luo, J. Intrauterine Adhesions Assessment by Photoacoustic Imaging versus High Frequency Ultrasound Imaging in Rats. *Biochemical and Biophysical Research Communications* **2024**, *741*, 151037, doi:10.1016/j.bbrc.2024.151037.
167. Xia, Q.; Lv, S.; Xu, H.; Wang, X.; Xie, Z.; Lin, R.; Zhang, J.; Shu, C.; Chen, Z.; Gong, X. Non-Invasive Evaluation of Endometrial Microvessels via in Vivo Intrauterine Photoacoustic Endoscopy. *Photoacoustics* **2024**, *36*, 100589, doi:10.1016/j.pacs.2024.100589.
168. Chapron, C.; Marcellin, L.; Borghese, B.; Santulli, P. Rethinking Mechanisms, Diagnosis and Management of Endometriosis. *Nat. Rev. Endocrinol.* **2019**, *15*, 666–682, doi:10.1038/s41574-019-0245-z.
169. Hsu, A.L.; Khachikyan, I.; Stratton, P. Invasive and Noninvasive Methods for the Diagnosis of Endometriosis. *Clinical Obstetrics & Gynecology* **2010**, *53*, 413–419, doi:10.1097/GRF.0b013e3181db7ce8.
170. Lin, W.; Hyeon, T.; Lanza, G.M.; Zhang, M.; Meade, T.J. Magnetic Nanoparticles for Early Detection of Cancer by Magnetic Resonance Imaging. *MRS Bull.* **2009**, *34*, 441–448, doi:10.1557/mrs2009.120.
171. Kaspute, G.; Bareikiene, E.; Prentice, U.; Uzieliene, I.; Ramasauskaite, D.; Ivaskiene, T. A Comprehensive Review of Advanced Diagnostic Techniques for Endometriosis: New Approaches to Improving Women's Well-Being. *Medicina* **2024**, *60*, 1866, doi:10.3390/medicina60111866.
172. Ding, Y.; Zhang, M.; Lang, J.; Leng, J.; Ren, Q.; Yang, J.; Li, C. *In Vivo* Study of Endometriosis in Mice by Photoacoustic Microscopy. *J. Biophotonics* **2015**, *8*, 94–101, doi:10.1002/jbio.201300189.

 doi:10.20944/preprints202603.1150.v1

173. Marquardt, R.M.; Nafiujjaman, M.; Kim, T.H.; Chung, S.-J.; Hadrick, K.; Kim, T.; Jeong, J.-W. A Mouse Model of Endometriosis with Nanoparticle Labeling for In Vivo Photoacoustic Imaging. *Reprod. Sci.* **2022**, *29*, 2947–2959, doi:10.1007/s43032-022-00980-5.
174. Lv, Q.; Zhang, Y.; Yang, R.; Dai, Y.; Lin, Y.; Sun, K.; Xu, H.; Tao, K. Photoacoustic Imaging Endometriosis Lesions with Nanoparticulate Polydopamine as a Contrast Agent. *Adv. Healthc. Mater.* **2024**, *13*, 2302175, doi:10.1002/adhm.202302175.
175. Yan, Y.; Basij, M.; Garg, A.; Varrey, A.; Alhousseini, A.; Hsu, R.; Hernandez-Andrade, E.; Romero, R.; Hassan, S.S.; Mehrmohammadi, M. Spectroscopic Photoacoustic Imaging of Cervical Tissue Composition in Excised Human Samples. *PLoS ONE* **2021**, *16*, e0247385, doi:10.1371/journal.pone.0247385.
176. Akins, M.L.; Luby-Phelps, K.; Bank, R.A.; Mahendroo, M. Cervical Softening During Pregnancy: Regulated Changes in Collagen Cross-Linking and Composition of Matricellular Proteins in the Mouse1. *Biology of Reproduction* **2011**, *84*, 1053–1062, doi:10.1095/biolreprod.110.089599.
177. Mahendroo, M. Cervical Remodeling in Term and Preterm Birth: Insights from an Animal Model. *Reproduction* **2012**, *143*, 429–438, doi:10.1530/REP-11-0466.
178. Basij, M.; Karpiouk, A.; Winer, I.; Emelianov, S.; Mehrmohammadi, M. Dual-Illumination Ultrasound/ Photoacoustic System for Cervical Cancer Imaging. *IEEE Photonics J.* **2021**, *13*, 1–10, doi:10.1109/JPHOT.2020.3043685.
179. Yan, Y.; Gomez-Lopez, N.; Basij, M.; Shahvari, A.V.; Vadillo-Ortega, F.; Hernandez-Andrade, E.; Hassan, S.S.; Romero, R.; MehrMohammadi, M. Photoacoustic Imaging of the Uterine Cervix to Assess Collagen and Water Content Changes in Murine Pregnancy. *Biomed. Opt. Express* **2019**, *10*, 4643, doi:10.1364/BOE.10.004643.
180. Markel, A.C.; Puri, V.; Domingo, M.J.E.; Miller, K.S.; Bayer, C.L. Spectral Photoacoustic Imaging of Age-Related Reproductive Tract Collagen Changes in a Mouse Model of Prolapse. *Photoacoustics* **2026**, *48*, 100810, doi:10.1016/j.pacs.2026.100810.
181. Kamath, S.D.; Ray, S.; Mahato, K.K. Photoacoustic Spectroscopy of Ovarian Normal, Benign, and Malignant Tissues: A Pilot Study. *J. Biomed. Opt.* **2011**, *16*, 067001, doi:10.1117/1.3583573.
182. Lin, Y.; Wang, L.; Hagemann, I.S.; Kuroki, L.M.; Sanders, B.E.; Hagemann, A.R.; Siegel, C.; Powell, M.A.; Zhu, Q. Vascular Graph Network for Ovarian Lesion Classification Using Optical-Resolution Photoacoustic Microscopy. *Photoacoustics* **2026**, *47*, 100794, doi:10.1016/j.pacs.2025.100794.
183. Leng, X.; Kou, S.; Lin, Y.; Hagemann, A.R.; Hagemann, I.S.; Thaker, P.H.; Kuroki, L.M.; McCourt, C.K.; Mutch, D.G.; Siegel, C.; et al. Quantification of Ovarian Lesion and Fallopian Tube Vasculature Using Optical-Resolution Photoacoustic Microscopy. *Sci. Rep.* **2022**, *12*, 15850, doi:10.1038/s41598-022-19778-1.
184. Nie, H.; Luo, H.; Chen, L.; Zhu, Q. A Coregistered Ultrasound and Photoacoustic Imaging Protocol for the Transvaginal Imaging of Ovarian Lesions. *JoVE* **2023**, 64864, doi:10.3791/64864.
185. Gröhl, J.; Hacker, L.; Cox, B.T.; Dreher, K.K.; Morscher, S.; Rakotondrainibe, A.; Varray, F.; Yip, L.C.M.; Vogt, W.C.; Bohndiek, S.E. The IPASC Data Format: A Consensus Data Format for Photoacoustic Imaging. *Photoacoustics* **2022**, *26*, 100339, doi:10.1016/j.pacs.2022.100339.
186. Gröhl, J.; Schellenberg, M.; Dreher, K.; Maier-Hein, L. Deep Learning for Biomedical Photoacoustic Imaging: A Review. **2020**, doi:10.48550/ARXIV.2011.02744.
187. Zhao, T.; Desjardins, A.E.; Ourselin, S.; Vercauteren, T.; Xia, W. Minimally Invasive Photoacoustic Imaging: Current Status and Future Perspectives. *Photoacoustics* **2019**, *16*, 100146, doi:10.1016/j.pacs.2019.100146.